Compositional modeling of three-phase flow with gravity using higher-order finite element methods

Joachim Moortgat,[1] Shuyu Sun,[2] and Abbas Firoozabadi[1,3]

[1] A wide range of applications in subsurface flow involve water, a nonaqueous phase liquid (NAPL) or oil, and a gas phase, such as air or CO_2. The numerical simulation of such processes is computationally challenging and requires accurate compositional modeling of three-phase flow in porous media. In this work, we simulate for the first time three-phase compositional flow using higher-order finite element methods. Gravity poses complications in modeling multiphase processes because it drives countercurrent flow among phases. To resolve this issue, we propose a new method for the upwinding of three-phase mobilities. Numerical examples, related to enhanced oil recovery and carbon sequestration, are presented to illustrate the capabilities of the proposed algorithm. We pay special attention to challenges associated with gravitational instabilities and take into account compressibility and various phase behavior effects, including swelling, viscosity changes, and vaporization. We find that the proposed higher-order method can capture sharp solution discontinuities, yielding accurate predictions of phase boundaries arising in computational three-phase flow. This work sets the stage for a broad extension of the higher-order methods for numerical simulation of three-phase flow for complex geometries and processes.

Citation: Moortgat, J., S. Sun, and A. Firoozabadi (2011), Compositional modeling of three-phase flow with gravity using higher-order finite element methods, *Water Resour. Res.*, *47*, W05511, doi:10.1029/2010WR009801.

1. Introduction

[2] A number of problems of high interest in hydrology and reservoir engineering involve multicomponent, three-phase flow in porous media. One example is the remediation of groundwater reservoirs contaminated with dense or light NAPL through air sparging. A second important process is the storage of industrial CO_2 in water flooded oil reservoirs, while increasing oil recovery.

[3] Species transfer between the phases affects the phase behavior and may change the phase densities and viscosities. This is important in the context of secure CO_2 sequestration. If injected CO_2 forms a gas cap, leakage could occur when the integrity of the cap rock is compromised [*Kopp et al.*, 2010]. However, under subsurface conditions CO_2 has a significant solubility in both water and oil. Furthermore, the mixture may have a higher density [*Ashcroft and Ben Isa*, 1997; *Simon et al.*, 1978], which affects the flow path [*Nasrabadi and Firoozabadi*, 2009] and may result in convective mixing [*Xu et al.*, 2006; *Farajzadeh et al.*, 2008; *Rongi et al.*, 2010; *Pau et al.*, 2010]. As a result, relatively high concentrations of CO_2 can be mixed efficiently throughout the liquid domain with little risk of leakage into the atmosphere or aquifers above [*Firoozabadi and Cheng*, 2010].

[4] The literature on multicomponent three-phase modeling related to water resources is relatively limited. *Niessner and Helmig* [2007, 2009] propose an interesting higher-order, multiphase, multiscale scheme. The third phase (NAPL), however, is assumed immobile and acts only as a source for mass transfer, making the dynamical problem essentially two-phase. Furthermore, densities are assumed constant, flow is incompressible and gravity and capillarity are neglected. An integral finite difference method was developed for water, air, and organic chemical phases by *Falta et al.* [1992] and for more general multicomponent organic contaminants in the work of *Adenekan et al.* [1993]. Other three-phase models have been developed in the field of reservoir engineering. However, the available models generally use first-order finite difference or finite volume methods to update mass transport [*Chang et al.*, 1998; *Guler et al.*, 2001; *Wang et al.*, 2003] and/or are restricted to incompressible flow, noncompositional fluids or black oil [*Geiger et al.*, 2009], three components, no gravity, or one-dimensional domains.

[5] As the number of phases and dimensions increases, numerical diffusion may mask physics in numerical simulation. For a process such as CO_2 injection in water-flooded reservoirs, basic mechanisms should be represented properly. This is a challenge in first-order methods due to numerical diffusion, grid orientation effects, and inaccuracies in the flux calculation. Higher-order methods such as the combined discontinuous Galerkin (DG) and mixed hybrid finite element (MHFE) are potentially very powerful for accurate simulation.

---

[1]Reservoir Engineering Research Institute, Palo Alto, California, USA.

[2]King Abdullah University of Science and Technology, Thuwal, Saudi Arabia.

[3]Department of Chemical and Environmental Engineering, Yale University, New Haven, Connecticut, USA.

[6] In the past, it has been shown that in two-phase flow, high-order MHFE-DG methods in addition to computational efficiency also have inherent advantages compared to first-order methods to represent physics of flow in complex geometries and for complex processes [*Hoteit and Firoozabadi*, 2006a]. These advantages include (1) low numerical diffusion and reduced grid orientation effects, (2) accurate flux calculation, (3) ease of implementation for anisotropic media, (4) multiphase flow representation in fractured media, (5) massively parallelizable, and (6) automatic element-wise conservation of mass.

[7] Earlier work in higher-order modeling of two-phase water-oil flow was based on the assumption of incompressibility [*Hoteit and Firoozabadi*, 2008]. For gas-oil mixtures, two-phase flow was formulated to allow for compressibility, phase behavior effects, and physical diffusion in fractured media. Promising results in two-phase flow have set the stage for numerical modeling in three-phase flows.

[8] In this work, we simulate for the first time, compressible three-phase flow based on the combined DG and MHFE methods, using the unified approach of volume balance of *Acs et al.* [1985]. We allow for the transfer of species between gas and oil phases and use the Peng-Robinson equation of state to model oil-gas phase behavior. However, we assume that water does not split in the gas and oil phases and that components from the oil and gas phases do not dissolve in water phase. This is a reasonable assumption in problems related to, for instance, improved oil recovery, when the connate water saturation is low and solubility of CO_2 in oil much higher than in water. The solubility of CO_2 in water is less than 3 mole percent under most reservoir conditions. In this paper, we lay the foundations for the higher-order finite element three-phase flow model. Mass transfer between all three phases requires complex stability and three-phase flash phase splitting algorithms that are the subject of a separate forthcoming publication, and can readily be incorporated in the model presented in this work.

[9] In the context of CO_2 sequestration in saline aquifers, even a low solubility of CO_2 in water has important implications. The reservoir pressure would increase steeply if CO_2 did not dissolve in water and simply formed a gas bubble in the top of the reservoir. A large body of literature is devoted to risk analysis studies of cap rock integrity and leakage in such a scenario. We conclude this paper by presenting one example, related to CO_2 sequestration, that does consider the CO_2 solubility in water. Because carbon sequestration is a two-phase problem, there is no need for three-phase flash algorithms.

[10] Even when CO_2 solubility is taken into account, the prospects of CO_2 sequestration may look bleak when an inaccurate equation of state is used, and diffusion is neglected. If CO_2 were only to dissolve at the interface between a gas cap and the aquifer, the storage capacity would be barely more than without solubility. However, CO_2 has the unique property that, when it dissolves in water, it increases the density of the aqueous phase, which has far-reaching consequences for CO_2 sequestration.

[11] When CO_2 is injected in the top of an aquifer at a low rate compared to the vast sizes of water aquifers, it slowly dissolves in the water through Fickian diffusion. Because the local density of the water-CO_2 mixture is higher than pure water below, the system becomes gravitationally unstable, causing inverse buoyancy of the mixture to the bottom of the reservoir. This convective mixing transports CO_2 throughout the domain at a significantly higher rate than diffusion alone would. This diffusion-convection mechanism may increase the CO_2 composition throughout large parts of the domain before any significant gas cap is formed. As a result, the storage capacity of water aquifers and risk of leakage may be substantially more favorable than what one would predict when some of the relevant phase behavior is neglected [*Firoozabadi and Cheng*, 2010].

[12] The occurrence of gravitational fingering due to the density increase of the aqueous phase is recognized and has been modeled by a number of authors [see, e.g., *Pau et al.*, 2010]. Further improvements can be made by considering higher-order accurate methods and, more importantly, by using an accurate equation of state. We will present a numerical example in which we use for the first time the cubic plus association (CPA) equation of state [*Li and Firoozabadi*, 2009] and our higher-order finite element methods to simulate CO_2 sequestration.

[13] In the presentation of the three-phase model, we consider CO_2 injection at relatively low rates in homogeneous media and neglect for the time being molecular diffusion (except in the two-phase carbon sequestration example), mechanical dispersion, and capillary pressure. The latter is a reasonable assumption when considering CO_2 injection in hydrocarbon reservoirs due to the low interfacial tension at high reservoir pressures [*Firoozabadi et al.*, 1988a] and the high solubility of CO_2 in the oil. In fractured and highly heterogeneous media, these assumptions are generally not valid and will be relaxed in future work.

[14] The paper is organized as follows. We first review the governing equations for three-phase compositional flow in porous media, which include Darcy's law, species transport equations, and modeling of the phase and volumetric behavior. We then formulate our iterative IMplicit Pressure Explicit Concentrations (IMPEC) scheme based on the combined DG and MHFE methods. We present numerical examples to demonstrate the modeling capabilities of our approach. In particular, we use our simulations to study CO_2 sequestration and compare different oil recovery scenarios of CO_2 injection following water flooding. We conclude the paper with various remarks.

2. Mathematical Model

[15] The main modeling equations for isothermal compositional three-phase flow in porous media consist of transport equations for each species, Darcy's law for the velocity of each of the phases, a pressure equation derived from volume balance, and thermodynamic equilibrium between the phases. These equations are supplemented with boundary conditions, constraint relations and expressions for viscosity, relative permeabilities, total compressibility, and partial molar volumes.

2.1. Species Transport Equations

[16] The equations that model the transport of species are obtained from the material balance of each species:

$$\phi \frac{\partial c z_i}{\partial t} + \nabla \cdot \vec{U}_i = F_i, \quad i = 1, \dots, n_c, \tag{1}$$

$$\vec{U}_i = \sum_{\alpha=w,o,g} c_\alpha x_{i,\alpha} \vec{\vartheta}_\alpha. \tag{2}$$

We denote porosity by ϕ and the overall molar density by c. We use $\alpha = w, o, g$ as the phase index, where the superscripts w, o, and g refer to water, oil, and gas phases. The index i labels the components or species, where n_c is the total number of components in the mixture and z_i and $\vec{U}_i$ are the overall mole fraction and overall molar flux of component i, respectively. For each phase α, $x_{i,\alpha}$ is the mole fraction of component i, $c_{,\alpha}$ is the molar density, and $\vec{\vartheta}_\alpha$ is the volumetric phase flux. F_i is the source term, which can be used to represent the well flow rate per unit volume.

[17] Fickian diffusion can be included as an additional flux term in $\vec{U}_i$ (using a mixed approach) as in the work of *Moortgat and Firoozabadi* [2010] but will be neglected here for clarity of presentation, as is mechanical dispersion.

2.2. Darcy's Law

[18] The phase flux $\vec{\vartheta}_\alpha$ for each phase $\alpha = w, o, g$ is given by Darcy's law for multiphase flow:

$$\vec{\vartheta}_\alpha = -\lambda_\alpha \mathrm{K}(\nabla p - \rho_\alpha \vec{g}), \quad \text{where} \quad \rho_\alpha = c_\alpha \sum_{i=1}^{n_c} x_{i,\alpha} M_i. \quad (3)$$

Here, p is the pressure, ρ_α is the mass density of phase α, $\vec{g}$ is the gravitational acceleration, and $\lambda_\alpha(S_\alpha)$ is the phase mobility. The mobility depends on the phase saturation, S_α; the relative permeability, $k_{r\alpha}(S_\alpha)$; and phase viscosity as $\lambda_\alpha(S_\alpha) = k_{r\alpha}(S_\alpha)/\mu_\alpha$. M_i is the molecular weight of component i and K is the absolute permeability tensor of the porous medium (but assumed scalar in the numerical examples presented in this paper).

[19] To model two- or three-phase flow, it is advantageous (see comments in section 3.3) to introduce the total volumetric flux (or total velocity)

$$\vec{\vartheta}_t = \sum_{\alpha=w,o,g} \vec{\vartheta}_\alpha = -\lambda_t \mathrm{K}\nabla p + \sum_{\alpha=w,o,g} \lambda_\alpha \rho_\alpha \mathrm{K}\vec{g}, \quad (4)$$

where we have introduced the total mobility λ_t. We will also use the fractional flow function f_α, which is the ratio of the mobility of phase α over the total mobility:

$$\lambda_t = \sum_{\alpha=w,o,g} \lambda_\alpha = \sum_{\alpha=w,o,g} \frac{k_{r\alpha}}{\mu_\alpha}, \quad (5)$$

$$f_\alpha = \frac{\lambda_\alpha}{\lambda_t}. \quad (6)$$

[20] The total velocity can be solved from the pressure equation (to be discussed below) and then the phase velocity can be computed by

$$\vec{\vartheta}_\alpha = f_\alpha \left(\vec{\vartheta}_t + \vec{G}_\alpha\right), \quad (7)$$

$$\vec{G}_\alpha = \sum_{\beta=w,o,g;\beta\neq\alpha} \lambda_\beta \left(\rho_\alpha - \rho_\beta\right) \mathrm{K}\vec{g}. \quad (8)$$

Equation (8) accounts for the contribution of gravity to the phase velocity and allows for countercurrent flow among phases. The countercurrent flow complicates the multiphase fluid dynamics and introduces various numerical challenges that we resolve in this paper (e.g. section 3.4).

2.3. Pressure Equation

[21] In this work we use the concept of total volume balance [*Acs et al.*, 1985; *Watts*, 1986] to represent the pressure equation in three-phase flow:

$$\phi C_f \frac{\partial p}{\partial t} + \sum_{i=1}^{n_c} \bar{v}_i \nabla \cdot \vec{U}_i = \sum_{i=1}^{n_c} \bar{v}_i F_i, \quad (9)$$

where C_f and $\bar{v}_i$ are the total compressibility and total partial molar volume for component i, respectively. In the past, the computation of C_f and $\bar{v}_i$ has been outlined for two-phase gas-oil mixtures [*Firoozabadi et al.*, 1988b]. We will provide working expression for three-phase gas-oil-water mixtures in this paper.

2.4. Equilibrium Calculations

[22] To simplify the equilibrium calculations for three-phase flow, we assume that the water component appears in the water phase only and that the water phase contains the water component only, which reduces the computation to oil-gas two-phase flash. To model carbon sequestration, we can include mass transfer between a CO_2 phase and the aqueous phase by a water-gas two-phase flash. Mass transfer between all phases can be incorporated by using a different flash routine in the MHFE-DG three-phase flow model presented in this work. The development of such three-phase stability and flash routines is the subject of a future publication. We denote the water component by index $i = 1$.

[23] The splitting of components between oil and gas phases is carried out by solving thermodynamic equilibrium equations at temperature T and pressure p for the fugacities $\mathcal{F}_{i,o}$ and $\mathcal{F}_{i,g}$ of component i in the oil and gas phases, respectively,

$$\mathcal{F}_{i,o}\left(T, p, x_{2,o}, \ldots, x_{n_c-1,o}\right) = \mathcal{F}_{i,g}\left(T, p, x_{2,g}, \ldots, x_{n_c-1,g}\right)$$
$$i = 2, \ldots, n_c, \quad (10)$$

together with mass balance equation for each component:

$$z_1 = \beta, \quad (11)$$

$$z_i = (1-\beta)\left((1-\gamma)x_{i,o} + \gamma x_{i,g}\right) \quad i = 2, \ldots, n_c, \quad (12)$$

and the constraint relations:

$$\sum_{i=1}^{n_c} x_{i,o} = \sum_{i=1}^{n_c} x_{i,w} = \sum_{i=1}^{n_c} x_{i,g} = \sum_{i=1}^{n_c} z_i = 1, \quad (13)$$

where γ is the gas phase mole fraction excluding water and β is the mole fraction of water in the mixture. We note that

$$x_{1,w} = 1, \quad (14)$$

$$x_{i,w} = 0, \quad \text{for} \quad i = 2, \ldots, n_c, \quad (15)$$

$$x_{1,g} = x_{1,o} = 0. \quad (16)$$

[24] The phase and volumetric behavior (including the calculations of the fugacities above) for the oil and gas phases are modeled by using the Peng- Robinson equation

of state [*Peng and Robinson*, 1976] with a volume translation to correct the oil phase density:

$$c_\alpha = \frac{p}{Z\alpha RT}, \tag{17}$$

$$Z_\alpha^3 - (1 - B_\alpha)Z_\alpha^2 + (A_\alpha - 3B_\alpha^2 - 2B_\alpha)Z_\alpha \\ - (A_\alpha B_\alpha - B_\alpha^2 - B_\alpha^3) = 0, \quad \alpha = o, g, \tag{18}$$

where R is the universal gas constant and A_α and B_α are the parameters of the Peng-Robinson equation of state. A_α and B_α are functions of pressure, temperature, and respective phase composition, which can be computed from mixing rules, binary interaction coefficients, and the critical properties and acentric factor of pure species (see *Firoozabadi* [1999] for details). The phase splitting algorithm is described in detail by *Moortgat and Firoozabadi* [2010] and uses an efficient combination of a successive substitution iterative (SSI) procedure (robust but relatively slow) and the Newton method (fast but needs sufficiently accurate initial guesses).

[25] The phase saturations can be expressed in terms of the molar densities as

$$S_w = \frac{\beta c}{c_w}, \quad S_g = (1 - \beta)\frac{\gamma c}{c_g}, \quad \text{and} \quad S_o = (1 - \beta)(1 - \gamma)\frac{c}{c_o}. \tag{19}$$

In this work, we express the isothermal water compressibility $C_{f,w}$ from

$$C_{f,w} \equiv \frac{1}{c_w}\frac{\partial c_w}{\partial p}, \tag{20}$$

and either interpolate the water molar density (and similarly, mass density) $c_w(p, T)$ (and $\rho_w(p, T)$) from experimental data [*Lemmon et al.*, 2010] or use the CPA EOS [*Li and Firoozabadi*, 2009].

[26] Assuming that there is no mass transfer between the water phase and the other two phases, we compute the total compressibility C_f (for the mixture) and the ith component's total partial molar volume $\bar{v}_i$ from $C_{f,w}$ and oil-gas volumetric properties by

$$C_f = S_w C_{f,w} + (1 - S_w)C_{f,og}, \tag{21}$$

$$\bar{v}_1 = \frac{1}{c_w}, \tag{22}$$

$$\bar{v}_i = \bar{v}_{i,og}, \quad i = 2, \ldots, n_c. \tag{23}$$

In the above equations, C_f, $C_{f,w}$, and $C_{f,og}$ are the total compressibility, the water phase compressibility, and the compressibility of combined oil and gas phases, respectively. Similarly, $\bar{v}_i$ and $\bar{v}_{i,og}$ are the ith component's total partial molar volume and its partial molar volume for the combined oil and gas phases, respectively. $C_{f,og}$ and $\bar{v}_{i,og}$ are computed as in previous work from the oil-gas phase-split calculations, using the Peng-Robinson equation of state.

2.5. Three-Phase Relative Permeabilities

[27] Relative permeabilities are a function of saturations and rock properties. Following Stone's methodology [*Stone*, 1970, 1973] (see also *Delshad and Pope* [1989]), we assume

that the water and gas relative permeabilities (k_{rw} and k_{rg}) are functions only of their own saturations. Thus k_{rw} and k_{rg} can be determined from two-phase relative permeabilities of the water-oil and oil-gas systems:

$$k_{rw}(S_w) = k_{rw}^0\left(\frac{S_w - S_{wc}}{1 - S_{wc} - S_{orw}}\right)^{n_w}, \tag{24}$$

$$k_{rg}(S_g) = k_{rg}^0\left(\frac{S_g - S_{gr}}{S_{g\max} - S_{gr}}\right)^{n_g}. \tag{25}$$

[28] Here $S_{g\max} = 1 - S_{wc} - S_{org}$, S_{wc} is either a connate or residual water saturation, S_{org} is the residual oil saturation to gas, S_{orw} is the residual oil saturation to water, and S_{gr} is the residual gas saturation (to both water and oil). Here k_{rw}^0 is the end point water relative permeability in the water-oil two-phase system (i.e., when $S_w = 1 - S_{orw}$), while k_{rg}^0 is the end point gas relative permeability in the oil-gas two-phase system.

[29] For the intermediate-wetting phase (oil phase), we take the following Stone I model, with similar meanings for the exponents n_{ow}, n_{og} and end points k_{row}^0, k_{rog}^0:

$$k_{row}(S_w) = k_{row}^0\left(\frac{1 - S_w - S_{orw}}{1 - S_{wc} - S_{orw}}\right)^{n_{ow}}, \tag{26}$$

$$k_{rog}(S_g) = k_{rog}^0\left(\frac{S_{g\max} - S_g}{S_{g\max} - S_{gr}}\right)^{n_{og}}. \tag{27}$$

[30] In two-phase regions, the pair of equations (24) and (26) describes oil-water systems, while equations (25) and (27) apply to oil-gas interaction. In regions where all three phases are present, the intermediate-wetting phase relative permeability is a normalized product of equations (26) and (27):

$$k_{ro}(S_w, S_g) = \frac{k_{row}k_{rog}}{k_{\text{norm}}}, \tag{28}$$

in terms of the following normalization variables (note that we only use equation (28) when both $S_w > 0$ and $S_g > 0$, so we always have $k_{\text{norm}} > 0$):

$$k_{\text{norm}} = k_{row}^0\frac{(1 - \overline{S}_w)(1 - \overline{S}_g)}{\overline{S}_o} \quad \text{, with}$$

$$b = 1 - \frac{S_g}{S_{g\max}},$$

$$S_{or} = bS_{orw} + (1 - b)S_{org},$$

$$\overline{S}_o = \frac{S_o - S_{or}}{1 - S_{wc} - S_{or} - S_{gr}},$$

$$\overline{S}_w = \frac{S_w - S_{wc}}{1 - S_{wc} - S_{or} - S_{gr}},$$

$$\overline{S}_g = \frac{S_g - S_{gr}}{1 - S_{wc} - S_{or} - S_{gr}}. \tag{29}$$

We note that phase behavior effects can complicate the relative permeabilities. In particular, evaporation of species from the oil to the gas phase may reduce the oil saturation

significantly below S_{org}. When evaporation is substantial, the residual oil to gas saturation loses its meaning, and we modify the original relations [*Stone*, 1970, 1973] by extrapolating to $S_{org} = 0$ when $S_o \ll S_{org}$, such that $S_{gmax} = 1 - S_w$ and always $S_g < S_{gmax}$.

[31] One may use relative permeabilities other than the one adopted here, such as those obtained by setting $k_{norm} = 1$. To find the phase viscosities, we use the method proposed by *Lohrenz et al.* [1964]. Together with proper boundary and initial conditions, the equations in this section form a mathematically complete system to model isothermal compositional three-phase flow in porous media.

3. Numerical Algorithms

[32] In this work, we decouple the system into two parts, a pressure equation involving the pressure and the total velocity and species transport equations to describe the evolution of compositions. The two parts are coupled using an iterative IMPEC approach. That is, we first solve the pressure equation implicitly by a mixed hybrid finite element (MHFE) method and then solve the species transport equations explicitly in time by the discontinuous Galerkin (DG) method. The maximum time step for the transport update is constraint by the Courant-Friedrichs-Lewy (CFL) condition [*Courant et al.*, 1928]. The implicit computation of the pressures is unconditionally stable but computationally expensive. The most efficient stable scheme is therefore to use multiple smaller time steps for the mass transport update per one larger time step for the pressure (and fluxes) update. In addition, a number of iterations for the entire coupled system can be carried out in each IMPEC step to improve the stability of time-splitting (for details, see *Delshad et al.* [2008a, 2008b, 2009]).

[33] The combined MHFE and DG methods have been successfully applied to a number of two-phase flow problems in porous media [*Hoteit and Firoozabadi*, 2005, 2006a, 2008, 2009; *Moortgat and Firoozabadi*, 2010], where powerful features of this combination have been demonstrated with a sequential IMPES or IMPEC formulation. A combined mixed finite element and discontinuous Galerkin method has also been applied to miscible displacement problems in porous media [*Sun et al.*, 2002], where a convergence analysis of the combined scheme was given. Mixed finite element has also been coupled with discontinuous Galerkin method through mortar finite elements [*Girault et al.*, 2008].

3.1. DG for Species Transport Equations

[34] We apply the DG method to solve the species transport equations. DG methods are specialized finite element methods that utilize discontinuous spaces to approximate solutions, with boundary conditions and interelement connectivity weakly imposed through bilinear forms [*Nitsche*, 1971; *Babuška*, 1973; *Babuška and Zlamal*, 1973; *Reed and Hill*, 1973; *Wheeler*, 1978; *Arnold*, 1982; *Cockburn et al.*, 2000; *Dawson et al.*, 2004; *Sun and Wheeler*, 2005a, 2005b, 2006]. A DG method is derived from variational principles by integration over local cells. Therefore the method is locally mass conservative by construction. In addition, because higher-order approximations are used within elements while element connectivity is weakly enforced through the bilinear form of DG, the

method has low numerical diffusion. With proper slope limiters, nonphysical oscillation in DG are suppressed. By using discontinuous approximation spaces, DG can be used when coefficients are highly nonlinear and can capture the discontinuity in the solution very well. Moreover, DG is efficiently implementable on unstructured and nonconforming meshes.

[35] The DG method consists of expanding the product of the molar density and compositions in terms of scalar shape functions φ_i (because the equations are identical for each species, we will drop the species index and denote $z = z_i$, etc., to avoid confusion with the discretization indices):

$$cz = \sum_{\mu} (cz)_{K,\mu}(t)\varphi_\mu(x,y), \quad c_\alpha x_\alpha = \sum_{\mu} (c_\alpha x_\alpha)_{K,\mu}(t)\varphi_\mu(x,y), \tag{30}$$

where the summations are over the μ degrees of freedom, which depend on the order of the approximation. The shape functions are taken from a standard DG space; that is, a globally discontinuous element-wise polynomial function space. In this work, we will consider rectangular meshes with bilinear shape functions that have the four nodal values as the degrees of freedom. We denote computational mesh elements by K (note that the symbol for the absolute permeability is K) and element edges by E.

[36] All fluxes (derived in the next section) are approximated by superpositions of the linear basis vector functions $\vec{w}_{K,E}$ of the lowest-order Raviart-Thomas space, RT_0 [*Raviart and Thomas*, 1977]. The coefficients are given by the normal components of the fluxes across element edges, denoted by $q_{K,E}$ for the total flux, and $q_{\alpha,K,E}$, $q_{K,E}^{Kg}$ for the phase and gravitational fluxes, respectively, with

$$\vec{\vartheta}_t(t,x) = \sum_{E \in \partial K} q_{K,E}(t)\vec{w}_{K,E}(x), \quad K \cdot \vec{g} = \sum_{E \in \partial K} q_{K,E}^{Kg} \vec{w}_{K,E}. \tag{31}$$

[37] For each discrete element, we obtain the weak form of equation (1) (with the phase fluxes given by equation (7)) by multiplying both sides by the same scalar test functions φ_j, integrating over the element and applying integration by parts to the convection term, to obtain the DG spatial discretization of the species transport equations:

$$\phi_K \sum_{\mu} \frac{d(cz)_{K,\mu}}{dt} \int_K \varphi_\mu \varphi_\nu - \sum_{\mu} \sum_{\alpha=w,o,g} \sum_{E \in \partial K} q_{\alpha,K,E}$$
$$\cdot \left[(c_\alpha x_\alpha)_{K,\mu} \int_K \varphi_\mu \vec{w}_E \cdot \nabla \varphi_\nu + \frac{(\widetilde{c_\alpha x_\alpha})_{K,E,\mu}}{|E|} \int_E \varphi_\mu \varphi_\nu \right]$$
$$= F_K \int_K \varphi_\nu, \tag{32}$$

where ϕ_K and F_K are the element-wise constant porosity and source term. The integrals over K denote L^2 inner products on an element and the integrals over ∂K, the L^2 inner product on the element faces (with surface/length $|E|$). The tilde is used throughout this work to denote the numerical fluxes that have to be constructed at element edges to project the discontinuous DG approximation for a variable into a globally continuous space (in this case to enforce mass

Table 1. Fluid Parameters for Example 1

Species	z_i^0	ω	T_c(K)	p_c(bar)	M_w(g/mole)	V_c(cm^3/g)
H$_2$O	0.5	–	–	–	18	–
C$_1$	0.0	0.01	190.6	46.0	16	6.15
C$_3$	0.5	0.15	369.8	42.48	44	4.54

conservation). For $(\widetilde{c_\alpha x_\alpha})_{K,E,\mu}$ we use the standard *upstream* value of $c_\alpha x_\alpha$ at node μ with respect to the normal component of the *phase* flux $q_{\alpha,K,E}$ through edge E:

$$
(\widetilde{c_\alpha x_\alpha})_{K,E,\mu} =
\begin{cases}
(c_\alpha x_\alpha)_{K,E,\mu}, & \text{when} \quad q_{\alpha,K,E} \geq 0, \\
(c_\alpha x_\alpha)_{K',E,\mu'}, & \text{when} \quad q_{\alpha,K,E} < 0,
\end{cases}
\tag{33}
$$

where K' and μ' refer to the element and nodes neighboring $E = \partial K \bigcup \partial K'$ and $\mu \in E$, respectively.

[38] We use the forward Euler method for the time integration of the species transport equations. High-order explicit time integration methods (such as second-order or fourth-order Runge-Kutta methods) are also feasible. To avoid unphysical oscillations in the numerical solution, we apply one of the standard slope limiters [see, e.g., *Hoteit and Firoozabadi*, 2006a] after each concentration step.

3.2. MHFE for the Pressure Equation

[39] We apply a mixed hybrid finite element (MHFE) method for the treatment of the pressure equation. The original mixed finite element methods [*Brezzi and Fortin*, 1991] are based on a variational principle expressing an equilibrium or saddle point condition that can be satisfied locally on each finite element, but it has an indefinite linear system of equations for the scalar variable (pressure) and the flux vector (total velocity). In the mixed hybrid finite element method, the linear system is made positive definite by appending as extra degrees of freedom the averaged pressures at the element edges. Also, in terms of these primary (auxiliary) pressure-trace variables, the size of the linear system is reduced by eliminating the fluxes and cell-averaged pressures.

[40] Approximation spaces for the MHFE method can be chosen to satisfy three important properties, local mass conservation, flux continuity, and the same order of convergence (and in some cases superconvergence) for both the scalar variable and the flux [*Ewing et al.*, 1991]. In the finite element setting, MHFE can readily accommodate full permeability tensors. By using a mixed formulation, the MHFE method is more accurate in flux calculation than the conventional finite volume and finite element methods. In particular, even though DG is superior to MHFE for convection-dominated problems, MHFE provides higher-order convergence for the flux variable than DG with the same degree of polynomials. With the MHFE method, we approximate simultaneously the pressure and velocity fields by discretizing individually the pressure equation and Darcy's law.

[41] First, we look at the pressure equation in terms of the total velocity:

$$
\phi C_f \frac{\partial p}{\partial t} + \sum_{i=1}^{n_c} \sum_{\alpha=w,o,g} \bar{v}_i \nabla \cdot c_\alpha x_{i,\alpha} f_\alpha \left(\vec{\vartheta}_t + \vec{G}_\alpha \right) = \sum_{i=1}^{n_c} \bar{v}_i F_i. \tag{34}
$$

The MHFE method consists of writing equation (34) in the weak form, where we will assume element-wise constant compressibility, partial molar volumes, and source terms. Also, we write $p_K = (\int_K p)/|K|$ for the element averaged pressure and use Gauss' theorem on the divergence term to obtain (restoring component index notation i):

$$
\phi C_{f,K} \frac{dp_K}{dt} + \sum_{i=1}^{n_c} \sum_{\alpha=w,o,g} \sum_{E \in \partial K} \bar{v}_{i_K} \int_E \widetilde{c_\alpha x_{i,\alpha}} f_\alpha \left(\vec{\vartheta}_t + \vec{G}_\alpha \right)
$$
$$
\cdot \vec{n}_E = \sum_{i=1}^{n_c} \bar{v}_{i,K} F_{i,K}. \tag{35}
$$

We note that the coefficient $c_\alpha x_{i,\alpha} f_\alpha$ is discontinuous across faces, similar to $c_\alpha x_{i,\alpha}$ in the mass transfer equation. To improve stability of the MHFE solution, we project $c_\alpha x_{i,\alpha} f_\alpha$ into a globally continuous space as $\widetilde{c_\alpha x_{i,\alpha}} f_\alpha$ before substituting into the above formulation for the pressure equation. The continuity postprocessing can be implemented by either using L^2 projection or using interpolation. In our simulations in this work, we modify the coefficient to a globally continuous element-wise linear (1-D) and bilinear (2-D) function by computing the average at interface centers and then applying linear interpolation (the same upwinding as in section 3.1 cannot be implemented because the phase fluxes are not known yet).

[42] The total velocity $\vec{\vartheta}_t$ in equation (35) is again expanded in the Raviart-Thomas basis vector functions equation (31) and we now use a backward Euler approximation of the time derivative to obtain an implicit scheme for the pressure field. Furthermore, in the iterative IMPEC scheme, a different (larger) time step can be used for the implicit update of equation (35) from the time step used in the explicit update of equation (32). Further details are similar to the appendix in the work of *Hoteit and Firoozabadi* [2006b].

3.3. Darcy's Law

[43] We now move to the MHFE discretization of Darcy's law. We multiply Darcy's law for the total velocity, equation (4), by $(\lambda_t K)^{-1}$:

$$
(\lambda_t K)^{-1} \vec{\vartheta}_t + \nabla p = \sum_{\alpha=w,o,g} f_\alpha \rho_\alpha K^{-1} K \vec{g}, \tag{36}
$$

where $K^{-1} K \vec{g}$ is left unevaluated to simplify the next equation. Note that, unlike the individual phase mobility, the total mobility is positive definite; thus its inverse always exists. This is also one of the reasons we select the total velocity as one of the primary unknowns. Another reason for the choice of the total velocity is that it is smoother than an individual phase velocity. The total molar flux can be used in place of the total volumetric flux [*Mikysta and Firoozabadi*, 2010], but we find the volumetric flux better behaved (numerically) than the molar flux.

[44] Multiplying a test vector function $\vec{w}_E$ to both sides of equation (36), expanding $\vec{\vartheta}_t$ and $K\vec{g}$ as in equation (31) and integrating the pressure gradient by parts, we have

$$
\sum_{E' \in \partial K} \left\{ \frac{q_{K,E'}}{\lambda_{K,t}} \int_K \left[\vec{w}_{K,E} \cdot K^{-1} \cdot \vec{w}_{K,E'} \right] + t p_{K,E} \right\} - p_K
$$
$$
= \sum_{\alpha=w,og} \sum_{E' \in \partial K} \left\{ q_{K,E'}^{Kg} f_{\alpha,K,E} \rho_{\alpha,K,E} \int_K \left[\vec{w}_{K,E} \cdot K^{-1} \cdot \vec{w}_{K,E'} \right] \right\}, \tag{37}
$$

Table 2. Relative Permeability and Other Relevant Parameters for Examples 1–4

Parameter	Example 1	Example 2	Example 3	Example 4
S_{wc}	0	0.1	0.1	0.1
S_{gr}	0	0.02	0.02	0.02
S_{orw}	0	0.4	0.4	0.4
S_{org}	0	0.1	0.1	0.1
S_{rw}^0	1	0.17	0.4	0.4
S_{rg}^0	1	0.63	0.63	0.63
S_{row}^0	1	0.69	0.69	0.69
S_{rog}^0	1	0.95	0.95	0.95
n_w	1	3	2	2
n_g	1	2	2	2
n_{ow}	1	2	2	2
n_{og}	1	2	2	2
k_{norm}	1	equation (29)	equation (29)	equation (29)
C_f	0	equation (20)	equation (20)	equation (20)
$p(t=0)$	69 bar	100 bar	277 bar	483 bar
T	311 K	344 K	403 K	400 K
ϕ	0.2	0.2	0.2	0.2
$\|K\|$	10 md	100 md	50 md	50 md

where $tp_{K,E} = \left(\int_E p \right)/|E|$ is the edge averaged pressure trace (further details can be found in the work of *Hoteit and Firoozabadi* [2006b]).

[45] We assume the domain to be defined by only Dirichlet and Neuman boundaries. On the latter, the normal components of the total velocity is imposed to vanish. In MHFE, the boundary pressure is imposed weakly through the weak formulation equation (37), while the boundary total velocity is imposed strongly by the construction of the velocity space (for details, see, e.g., *Brezzi and Fortin* [1991]). In our MHFE, however, both are imposed strongly.

[46] The discretizations of Darcy's law (for the total velocity) and the pressure equation lead to an algebraic system which can be used to uniquely determine the numerical solutions of pressure and total velocity. When the RT_0 space is used and flux continuity across element edges is imposed, the flux coefficients $q_{K,E}$ and cell averaged pressure p_K can be eliminated resulting in an algebraic system which only has the face average pressures as the unknowns. Since we use fluid properties from the previous time step, the resulting algebraic system is linear, and it can be solved by either a direct sparse linear solver (when the number of unknowns is not too large, roughly less than 100,000) or an iterative sparse linear solver (where the number of unknowns can be much larger). The cell averaged pressures and fluxes are subsequently found by simple back substitution in the remaining equations.

3.4. Subtleties Related to Gravity

[47] As was mentioned in section 3.1, the $\vec{G}_\alpha$ term in equation (7) allows for countercurrent flow among phases. This has important implications for the upwinding of mobilities in the phase flux calculations. This issue was briefly discussed by *Mikysta and Firoozabadi* [2010] for two-phase flow, but given its importance for the correct modeling of multiphase flow in a gravitational field, we will discuss this gravity effect in more detail. Upwinding in multiphase flow is straightforward in schemes where all phase fluxes are computed at the same time. However, in the MHFE method discussed in section 3.2, we only solve for the total flux. Complications arise in subsequently deriving the three phase fluxes using self-consistent upwind phase mobilities. The generalized upwinding scheme presented here is one of the key elements of this paper.

[48] The subtlety relates to the evaluation of equation (7). The total flux $\vec{\vartheta}_t$, or rather $q_{K,E}$, is derived from the MHFE method applied to Darcy's law and the pressure equation. This has the advantage that it automatically provides a vector field for the total flux that is continuous across element boundaries. However, the DG approximations of the phase mobilities and mass densities in equation (8) are discontinuous across element faces, so care has to be taken to guarantee mass conservation (continuity of the phase fluxes). One may be tempted to take the upwind values of the phase mobilities with respect to phase fluxes from the previous time step, similar to
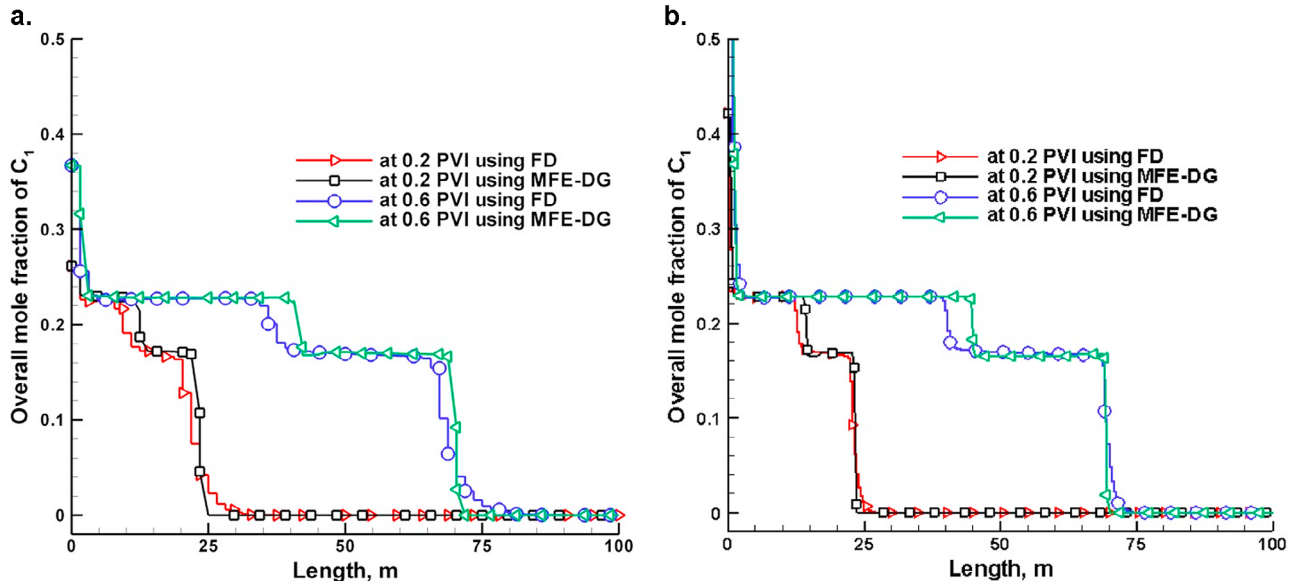

Figure 1. Example 1, showing the overall methane composition (mole fraction) at different PVIs from DG and FD with (a) 64 elements/nodes and with (b) 256 elements/nodes.
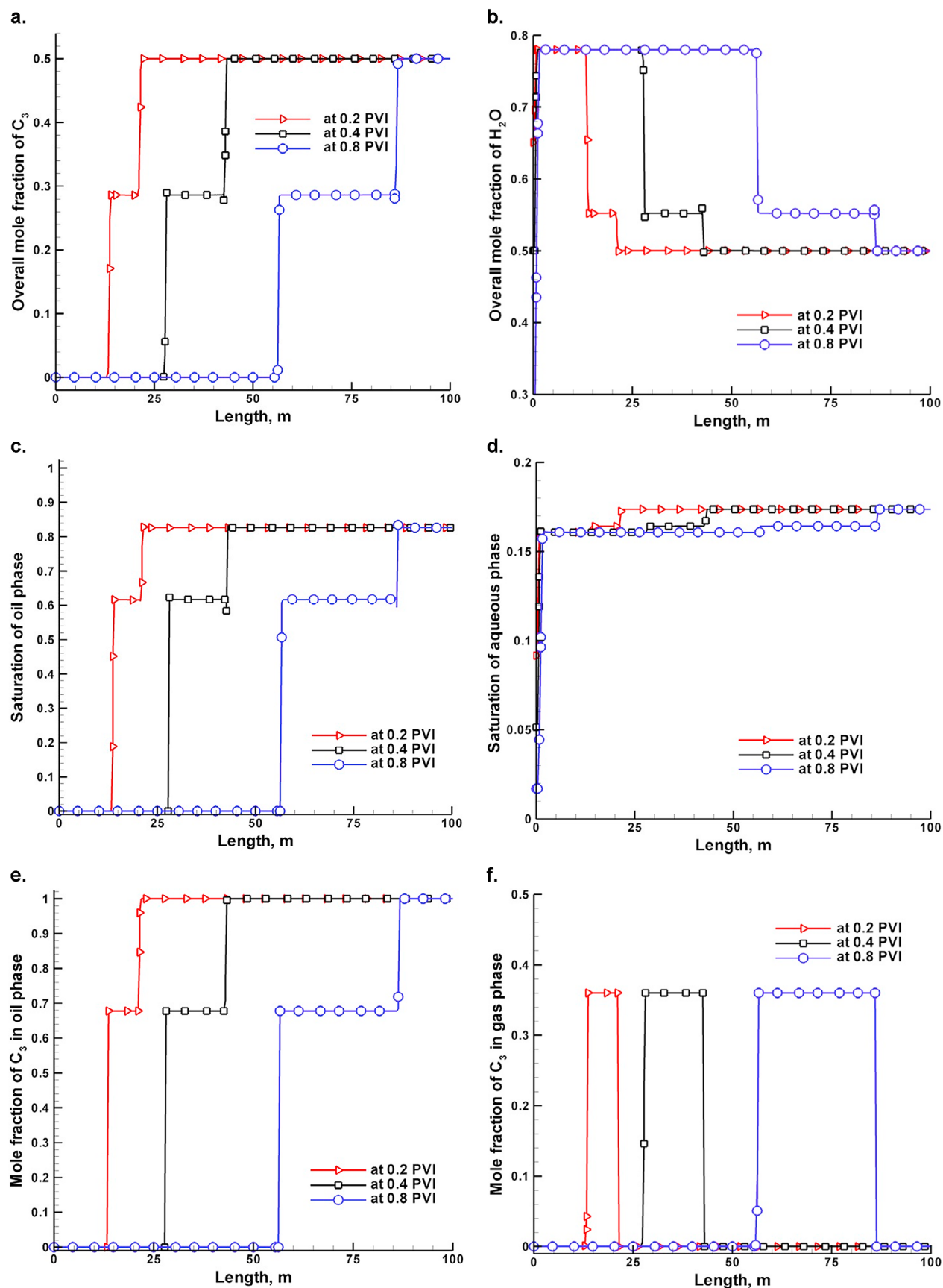
Figure 2. Example 1, showing the simulation results from DG with 256 elements for (a) overall molar fraction of propane, (b) overall molar fraction of water, (c) oil saturation, (d) water saturation, (e) molar fraction of propane in oil phase, and (f) molar fraction of propane in gas phase.
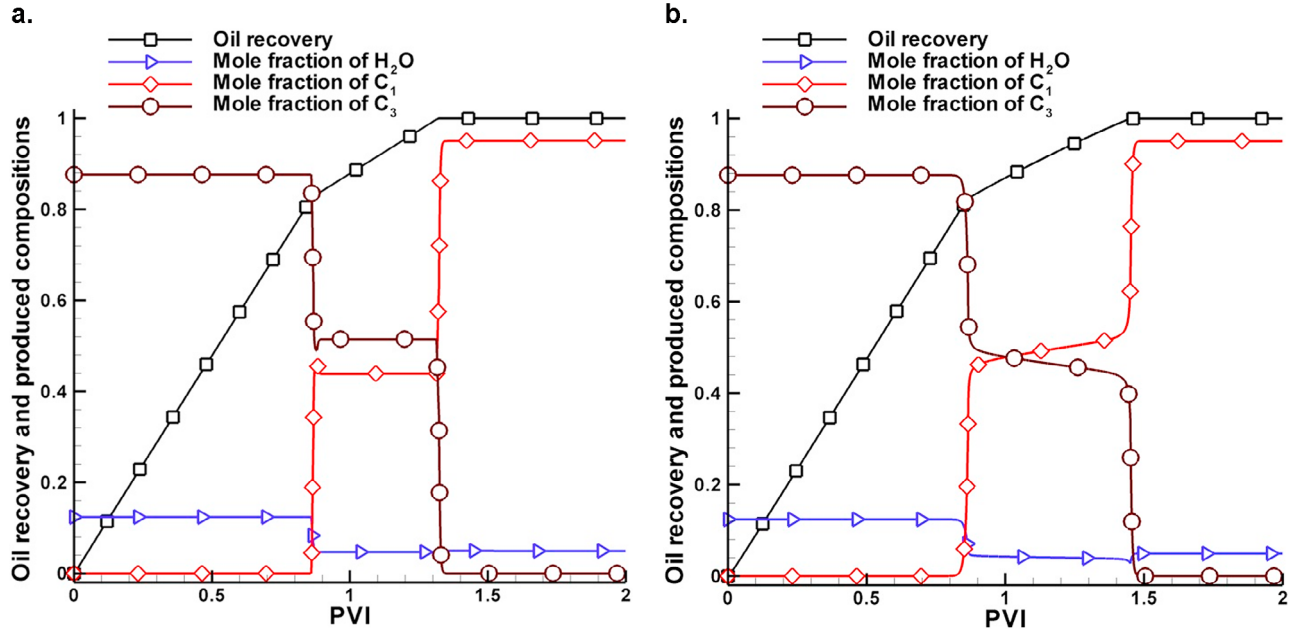
Figure 3. Example 1, showing oil recovery (molar fraction of propane produced) and overall composition of the produced fluid (in mole fractions) from (a) DG with 256 elements and (b) FD with 256 nodes.

the update of the mass transport equation. However, since the goal is to derive those phase fluxes, the upwind directions with respect to the phase fluxes are not known yet. Only in the absence of gravity (e.g., horizontal flow components) are the directions of the phase fluxes known a priori, as flowing in the same direction as the total flux.

[49] We propose the following solutions. From inspecting equation (8) it is clear that at each edge, the normal component of the gravity term is positive definite for one phase and negative definite for the other phase, depending on the sign of $K\vec{g} \cdot \vec{n}$. When the outward normal at the edge under consideration is downward, i.e., $K\vec{g} \cdot \vec{n} > 0$, then the gravity term is positive for the heaviest phase, negative for the lightest phase, and undetermined for the intermediate phase (and vice versa for the element neighboring the same edge, which will have its normal pointing upward).

[50] To find the upwind directions for all three phases, we suggest the following steps:

[51] 1. First, we pick the phase α_1 for which the phase flux has the same sign as the total flux. This is the heaviest phase when $(\vec{\vartheta}_t \cdot \vec{n})(K\vec{g} \cdot \vec{n}) > 0$ or the lightest phase when $(\vec{\vartheta}_t \cdot \vec{n})(K\vec{g} \cdot \vec{n}) < 0$. Even though we cannot yet evaluate the full expression for $\vec{\vartheta}_{\alpha_1}$, its sign determines the first upwind phase mobility $\tilde{\lambda}_{\alpha_1}$.

[52] 2. For the other two phases, not even the sign of the phase flux can be determined a priori, but since there are only two options we can try each and then check for consistency. We will denote by α_3 the "opposite" phase of α_1, meaning the lightest phase when α_1 is the heaviest and vice versa. The gravity term in equations (7) and (8) for α_3 always has the opposite sign of $\vec{\vartheta}_t$, so the sign of $\vec{\vartheta}_{\alpha_3}$ depends on the (unknown) relative magnitude of $\vec{\vartheta}_t$ and $\vec{G}_{\alpha_3}$. In this step, as a first guess we assume that $\vec{\vartheta}_{\alpha_3}$ has the same sign as $\vec{\vartheta}_{\alpha_1}$ and $\vec{\vartheta}_t$ and pick the upwind value of $\tilde{\lambda}_{\alpha_3}$ correspondingly.

[53] 3. With $\tilde{\lambda}_{\alpha_1}$ and $\tilde{\lambda}_{\alpha_3}$ we can now evaluate the sign of the phase flux of the intermediate-density phase α_2, and obtain $\tilde{\lambda}_{\alpha_2}$.

[54] 4. Next we check for consistency by using all three upwinded phase mobilities to fully evaluate $\vec{\vartheta}_{\alpha_3}$. If the resulting sign agrees with our initial guess in step 2, the process is complete; otherwise we repeat steps 2–4 starting from the opposite upwind choice for $\tilde{\lambda}_{\alpha_3}$ (which also affects $\tilde{\lambda}_{\alpha_2}$).

[55] 5. When the sign of $\vec{\vartheta}_{\alpha_3}$ is consistent with the choice of $\tilde{\lambda}_{\alpha_3}$, all upwind mobilities are known and the full expressions in equation (7) are evaluated.

[56] When one or two of the phases are not present, or on vertical element faces where $K\vec{g} \cdot \vec{n} = 0$, we revert to a simpler determination of the upwind directions.

4. Numerical Results

[57] We present five numerical examples of various degrees of complexity to illustrate features and strengths of the proposed model. In example 1, methane is injected in a 100 m long 1-D horizontal porous medium saturated with water and propane. The 1-D simulation for a three-component mixture most clearly illustrates the development of three shocks that separate single-phase, two-phase, and three-phase regions. Example 2 shows that the same features appear in a 100×100 m^2 2-D horizontal domain with a three-component water-CO_2-normal decane mixture. In examples 3 and 4, we study water flooding of a 2-D vertical

Table 3. Fluid Parameters for Examples 2 and 5

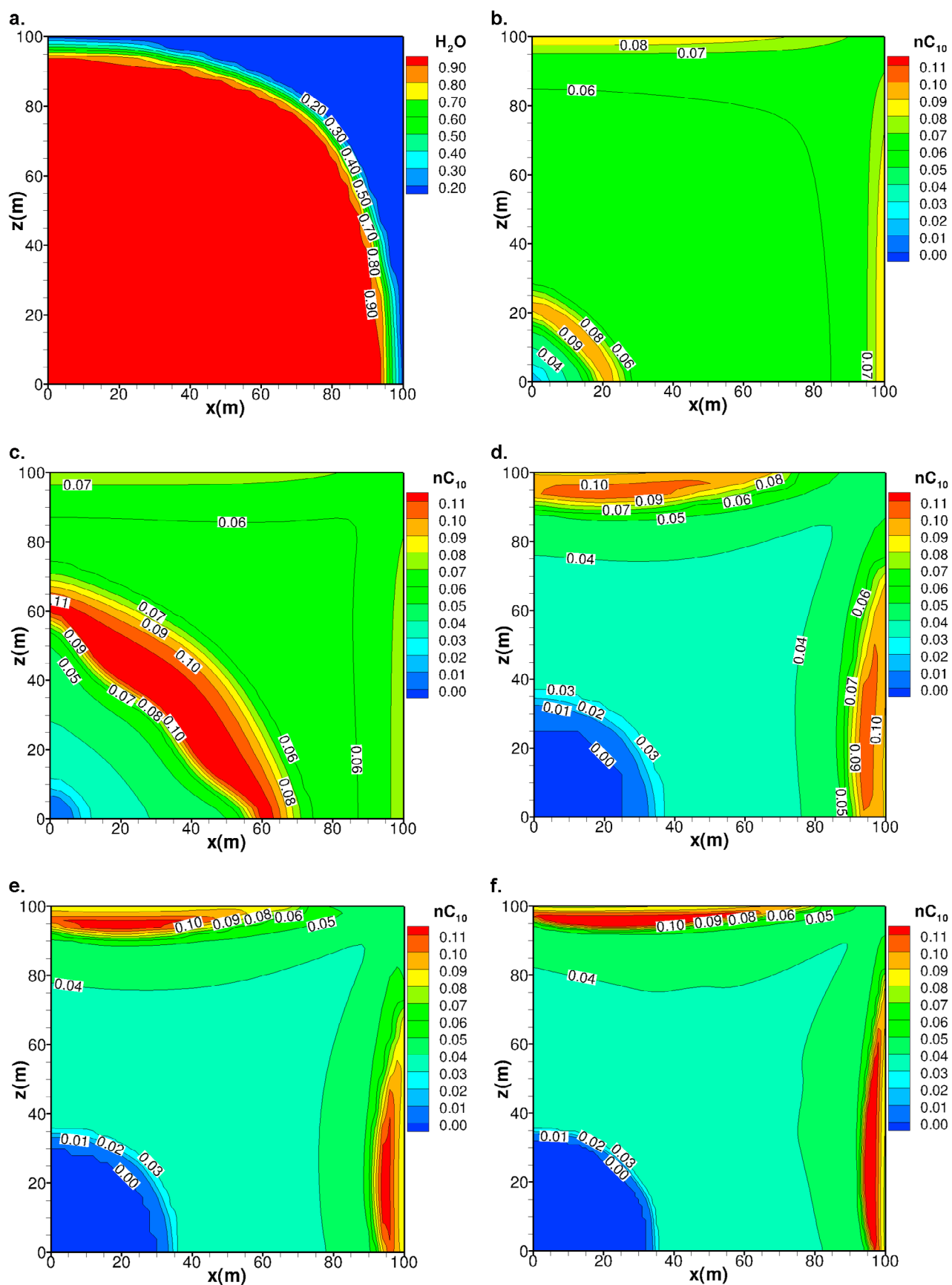| Species	z_i^0	ω	T_c(K)	p_c(bar)	M_w(g/mole)	V_c(cm^3/g)
H_2O	0.1	0.34	647.3	220.9	18	–
CO_2	0.0	0.24	304.1	73.8	44	2.14
nC_{10}	0.9	0.45	617.7	21.1	142	4.39

Figure 4. Example 2, showing (a) the overall molar fraction of water at 45% PVI of water and overall molar fraction of nC_{10} at (b) 2% PVI, (c) 10% PVI, and (d–f) 200% PVI of CO_2 injection. Computed on 32×32 (Figures 4a–4d), 50×50 (Figure 4e), and 100×100 (Figure 4f) size meshes.
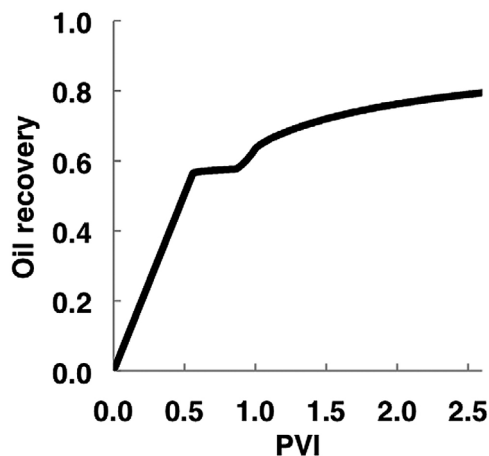
Figure 5. Example 2, showing the oil recovery (liquid volume fraction).

domain that is initially saturated with a multicomponent oil, followed by CO_2 injection. We study the effect of gravity by considering in example 3 an oil that is denser than the injected CO_2, and in example 4 one that is lighter than the CO_2. The final example considers some important aspects of carbon sequestration, where CO_2 solubility is accounted for. We incorporate a cubic plus association equation of state [*Li and Firoozabadi*, 2009] to accurately model the CO_2-water phase behavior. A density-increase of the aqueous phase results in more pronounced gravitational instabilities as compared to example 4.

[58] In all the examples, the porosity is 0.2 and we apply a constant volumetric injection rate in the injection well, while keeping the pressure constant at the production well. The (scalar) absolute permeability is 10 md in example 1, 100 md in examples 2, 50 md in examples 3 and 4, and 5000 md in example 5. The simulations are performed with the DG method for mass transport unless specified otherwise (some simulations are repeated using the FD for comparison). As mentioned in section 3.3, we assume impermeable domain boundaries except for the production well edges where a constant pressure is maintained. The injection wells are treated as a source term.

4.1. Example 1: Water-C_1-C_3 Mixture in Horizontal 1-D Domain

[59] In this example, we inject methane (C_1) at the left end into the medium, which is initially saturated with 50% of propane (C_3) and 50% of water (in mole fraction). The initial pressure is 69 bar, and the temperature is 311 K. The injection rate is 10% pore volume (PV) per year. Table 1 lists the mole fraction of components z_i^0 in the initial oil, and the acentric factor ω, critical temperature T_c, critical pressure p_c, molar weight M_w, and critical volume V_c (we do not consider a volume translation s in this example). Table 2 summarizes the relative permeability parameters, compressibility, initial pressure, temperature, porosity, and absolute permeability for all examples. In this example, we use linear relative permeabilities with unit normalization k_{norm}, and choose all residual and critical saturations to be zero. Water compressibility is neglected in this example.

[60] Figure 1 shows the simulation results for the overall mole fraction of methane versus the distance from the

injection point. Here we compare four simulations from our DG mass transport update and the conventional finite different method (FD) with 64 and 256 elements/nodes (both use MHFE for the pressures and fluxes). The DG solution with 256 elements firmly predicts three shocks that separate four regions. The first region from the left is the gas phase region, a very thin single-phase region starting from the injection point. The second region is the water-gas two-phase region that has a methane overall composition of roughly 0.23 mole fraction. The third region is the water-oil-gas three-phase region that has a methane overall composition of roughly 0.16. Finally the fourth region is the water-oil region, where the influence of the injected gas has not reached. The first shock from the left is the one that separates the gas and water-gas regions, and its propagation speed is slow due to the relatively large viscosity of water. The second (between the water-gas and three-phase regions) and the third (between three-phase and water-oil regions) shocks are developed due to the phase behavior effect. Because the mobility of the methane-rich gas phase is larger than that of the displaced fluid (propane-rich oil phase), the third shock moves faster than the second shock, which makes the three-phase region wider as time goes by. This difference in propagation speed stabilizes the three-phase region (if we assume otherwise that the speed of the third shock were slower than that of the second shock, the three-phase region would disappear).

[61] To capture shocks accurately, the numerical diffusion should be small. The FD method has a substantial numerical diffusion; it decreases as the number of nodes increases. The DG method, however, creates much less numerical diffusion. Comparison of the results in Figure 1 shows that the DG method even with 64 elements has slightly lower numerical diffusion than FD with 256 nodes. Numerical diffusion does not affect the location of the forefront shock (the third shock from the left), but it affects the predicted location of the inner miscibility front because the inaccuracy from resolving the phase behavior in the three-phase region can contaminate the computation of the downwind front. Consequently, the predicted location for the inner front is more accurate in DG than in FD. Note that the predicted inner front location from FD with 256 nodes is similar to that from DG with 64 elements.

[62] Figure 2 displays results computed from the DG method on 256 elements for the overall composition of each species, saturation of each phase and composition of species in each phase; all show discontinuities across shocks. Phase viscosity, phase molar density, total molar density, total compressibility, and a component's total partial molar volume, also have discontinuities (not shown). Discontinuous

Table 4. Fluid Parameters for Example 3

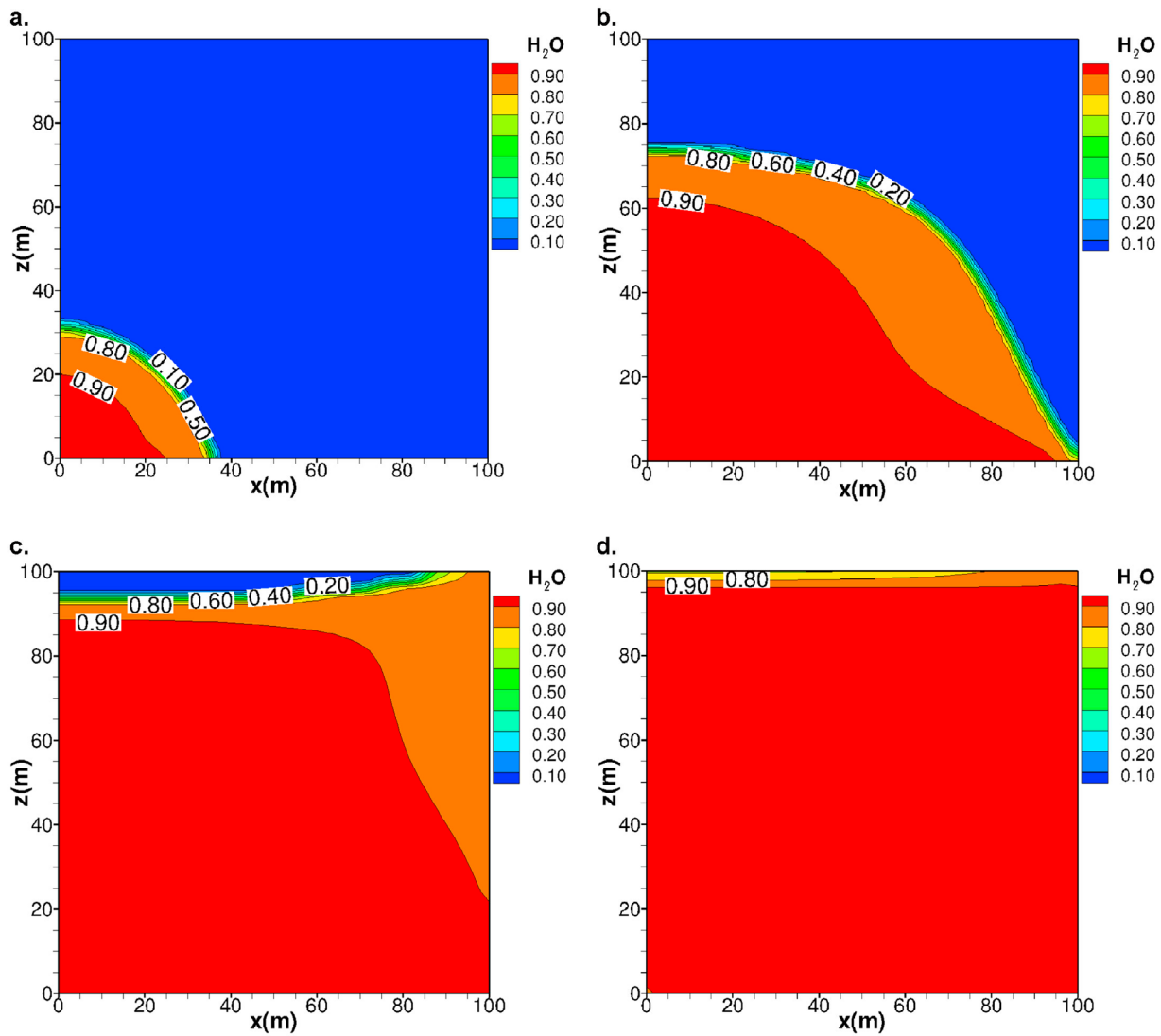| Species	z_i^0	ω	T_c (K)	p_c (bar)	M_w (g/mole)	V_c (cm³/g)	s
CO_2	0.008	0.24	304.1	73.8	44	2.14	0.06
N_2	0.003	0.04	126.2	33.9	28	3.21	−0.29
C_1	0.445	0.01	190.6	46.0	16	6.15	−0.15
C_2–C_3	0.121	0.12	327.8	46.5	35	4.74	−0.20
C_4–C_5	0.051	0.21	435.6	36.1	63	4.37	−0.06
C_6–C_{10}	0.133	0.42	574.4	25.0	116	4.25	0.05
C_{11}–C_{24}	0.166	0.66	709.0	15.0	219	4.10	0.15
C_{25+}	0.074	1.73	891.5	7.5	466	3.50	0.50

Figure 6. Example 3, showing the overall molar composition of water at (a) 5%, (b) 30%, (c) 60%, and (d) 100% PV water injection. Injection is from the bottom left corner and production is from the top right corner.

approximation spaces in DG clearly help to resolve the jumps numerically.

[63] Oil recovery (the molar fraction of C_3 extracted from the domain) and the compositions of the produced fluid are depicted in Figure 3 from both the DG and FD methods. The composition plots have discontinuities or sharp turning points when shocks exit the domain. The larger numerical diffusion of FD over DG is revealed from the predictions of methane and propane compositions in the produced fluids (the produced compositions from 80%–150% PVI in Figure 3).

4.2. Example 2: Water-CO_2-nC_{10} Mixture in Horizontal 2-D Domain

[64] The interest in three-phase numerical modeling is largely related to CO_2 storage and CO_2 injection as an enhanced recovery mechanism in reservoirs that have been water flooded. To emphasize several specific aspects of water flooding followed by CO_2 injection, we start with a simplified example in which a 100×100 m^2 2-D horizontal

domain is initially saturated with 0.9 normal decane (nC_{10}) and 0.1 water mole fractions. The fluid properties and other relevant parameters, such as initial temperature (344.26 K) and pressure (100 bar), are listed in Tables 2 and 3. The
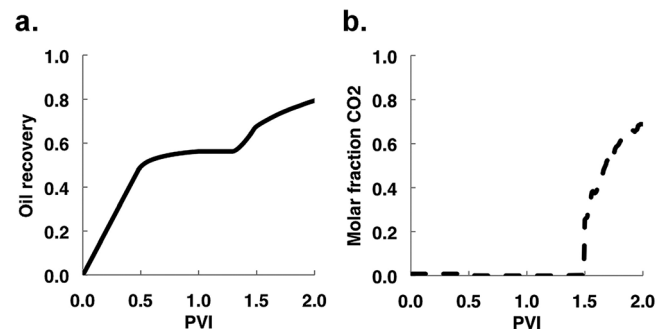
Figure 7. Example 3, showing (a) oil recovery and (b) overall CO_2 molar fraction in the production well.
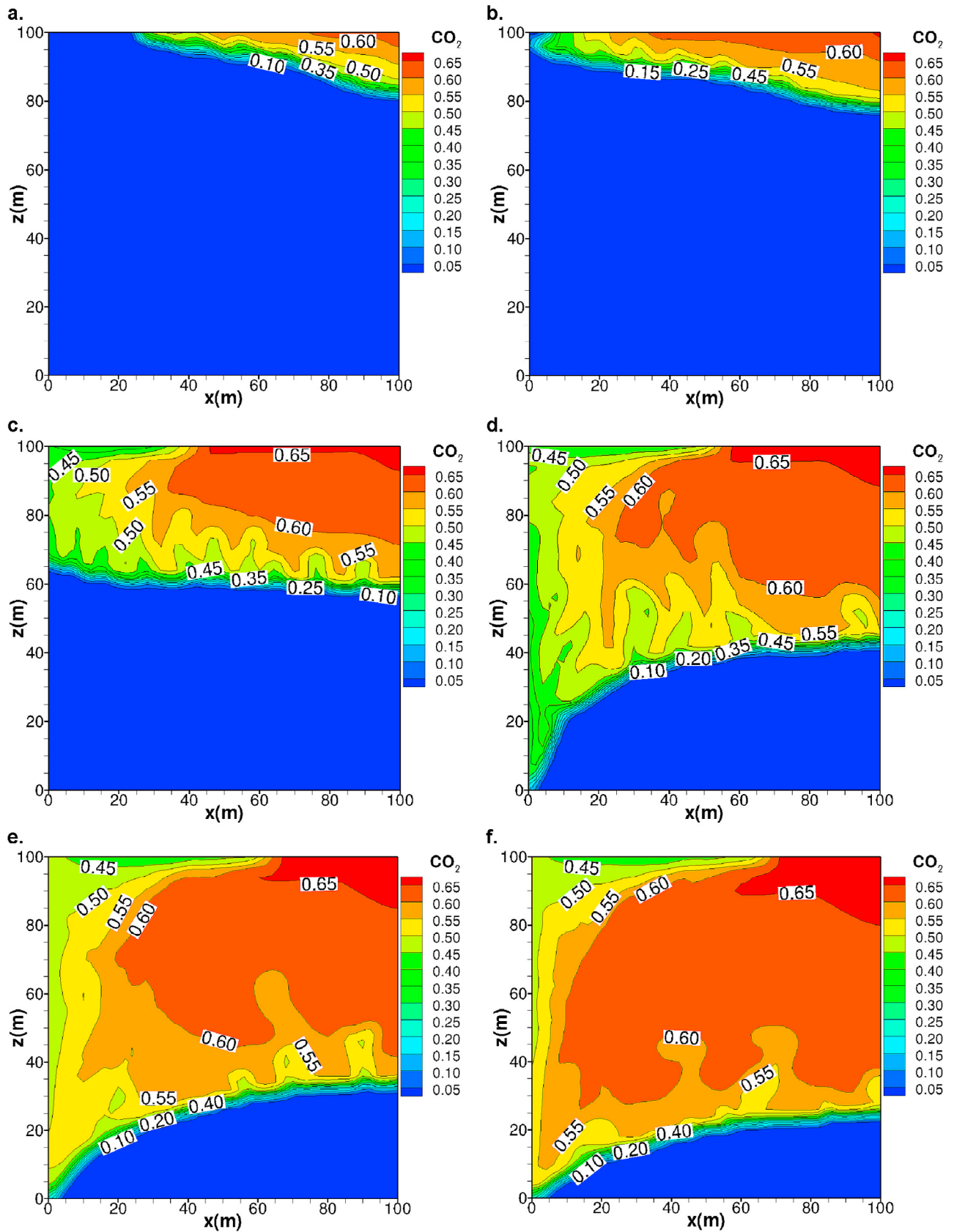
Figure 8. Example 3, showing the overall molar fraction of CO_2 at (a) 5%, (b) 10%, (c) 30%, (d) 50%, (e) 70%, and (f) 100% PV CO_2 injection.
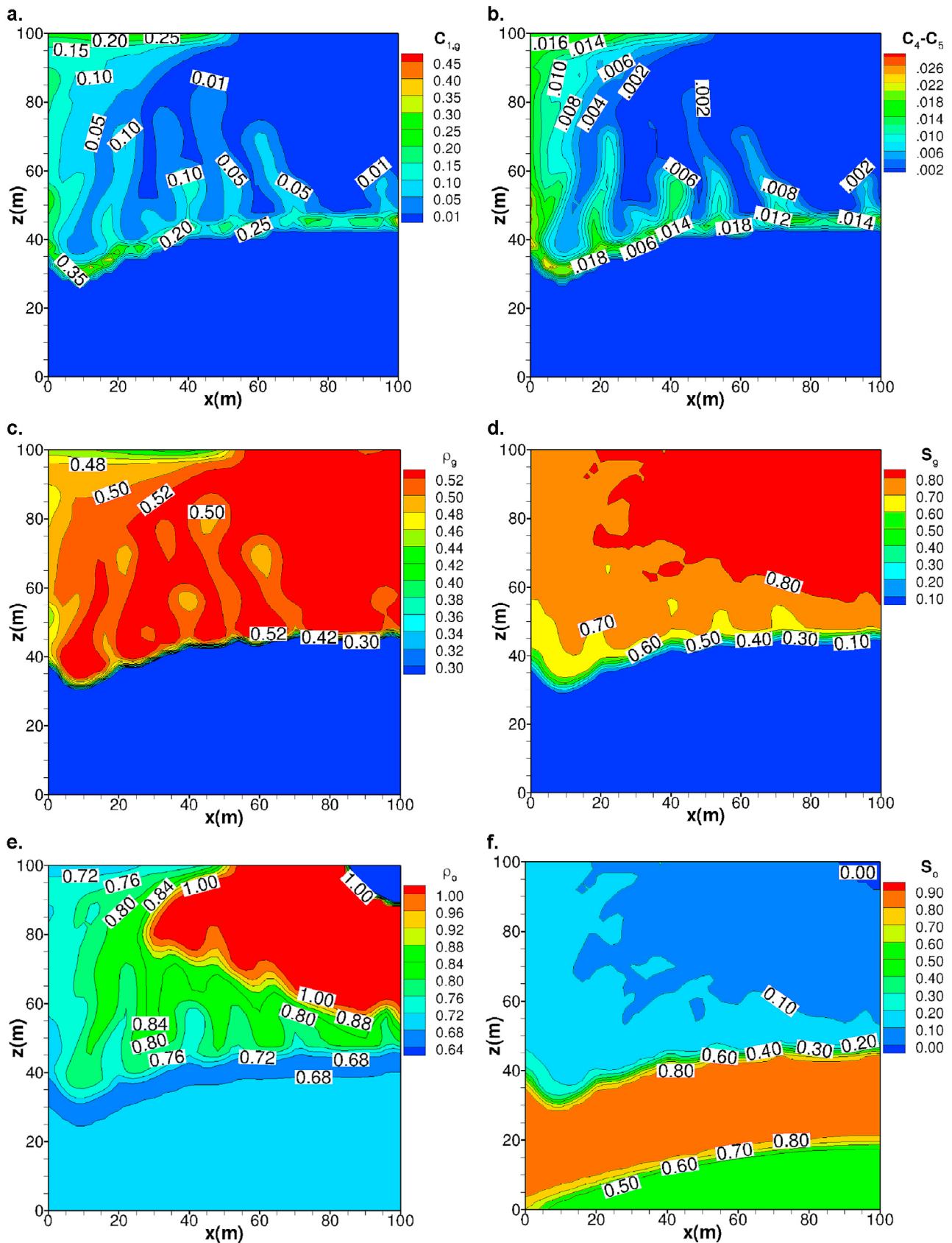
Figure 9. Example 3, showing various results at 45% PV CO_2 injection: (a) molar fraction of methane in gas phase, (b) molar fraction of C_4-C_5 in gas phase, (c) density of gas phase in g/cm^3, (d) gas saturation, (e) density of oil phase in g/cm^3, and (f) oil saturation.
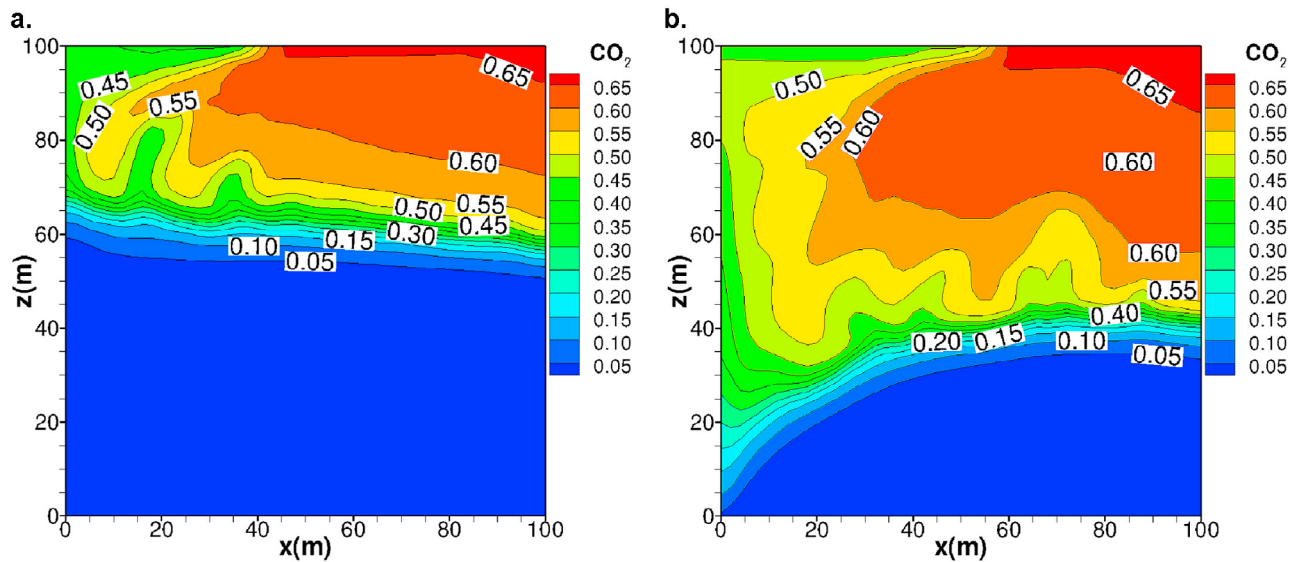
Figure 10. Example 3, showing the overall CO_2 molar composition computed with lowest-order FD at (a) 30% and (b) 50% PVI.

injection and production wells are in the bottom left and top right corners, respectively, and we use a 32×32 element rectangular grid.

[65] We first inject water at a constant rate of 10% PV/year for 6 years, efficiently displacing the nonresidual oil, as shown in Figure 4a after 45% PV water injection. Since water has a viscosity larger than the oil (decane), a shock is formed separating the oil-displaced region and the unaffected region. The thin width of the shock and its isotropic circular shape in the simulation indicate low numerical diffusion and low grid orientation effect of DG, respectively. After injecting 60% PV of water, further flooding does not lead to additional oil recovery, as shown in Figure 5 because the oil reaches the residual oil saturation to water of 0.4 (see Table 2), corresponding to an overall mole fraction of 0.06.

[66] We therefore switch to injecting CO_2 at the same rate for 20 years. Shortly after the start of CO_2 injection, a spike is formed in the plot of the overall mole fraction of decane (shown in Figure 4b). One reason for the formation of this spike is the change of the relative permeability after a new phase (gas) is introduced. Additionally, the spike formation is enhanced by the swelling of the oil phase due to the substantial dissolution of CO_2 into the oil phase. Because of the relative permeability effect and the oil swelling, the oil saturation increases above the original residual saturation, and then the oil phase starts to flow toward the pressure drop direction (diagonally to the top right corner). The convection of the decane component then causes its composition to increase downstream, thus forming a spike which becomes wider as it propagates (Figure 4c).

[67] We have examined the oil saturation and the decane component molar density as functions of distance from the injection point (not shown); they all exhibit a similar "spike," which confirms our explanation above. We have also examined the viscosity of oil phase (not shown) and found that it is reduced by more than two-fold with the dissolution of CO_2. This is another mechanism for the CO_2 improved oil recovery, where oil phase is mobilized sig-

nificantly by CO_2. The viscosity reduction also explains why the spike moves faster than the rest of the fluid mixture. Various authors have observed the spike predicted in our simulations in their experiments [*Leach and Yellig*, 1981; *Kremesec and Sebastian*, 1985].

[68] After the oil-swelling spike exits the system, the oil saturation returns back to the residual level and oil stops flowing. However, the oil component (decane) is still being extracted by a third mechanism, vaporization of decane into the gas phase. As the gas phase is always flowing, any decane vaporized into gas will be convected downstream, eventually reaching the production point. Figure 4d shows that after injecting two PV of CO_2, nearly all the decane has evaporated from a radius of ~35 m around the injection well. We continued the simulation for several more pore volumes of CO_2 injection (which would not be economical), to achieve complete recovery of decane due to the vaporization effect.

[69] To illustrate the convergence of these results, we repeat the simulation on two finer meshes of 50×50 and 100×100 elements, respectively. The nC_{10} composition at two PV CO_2 injection is given in Figures 4e and 4f, which show little further reduction in numerical diffusion compared to Figure 4d.

[70] In the next two examples, we will study a similar scenario but for two multicomponent reservoir oils and we will focus on the effect of gravity. The domain is the same as in example 2 but with an absolute permeability of 50 md and a 50×50 rectangular grid. In both examples we first inject one PV of water in 2.74 years from the bottom left corner of the domain (i.e., 0.1% PV/day) and produce

Table 5. Fluid Parameters for Example 4

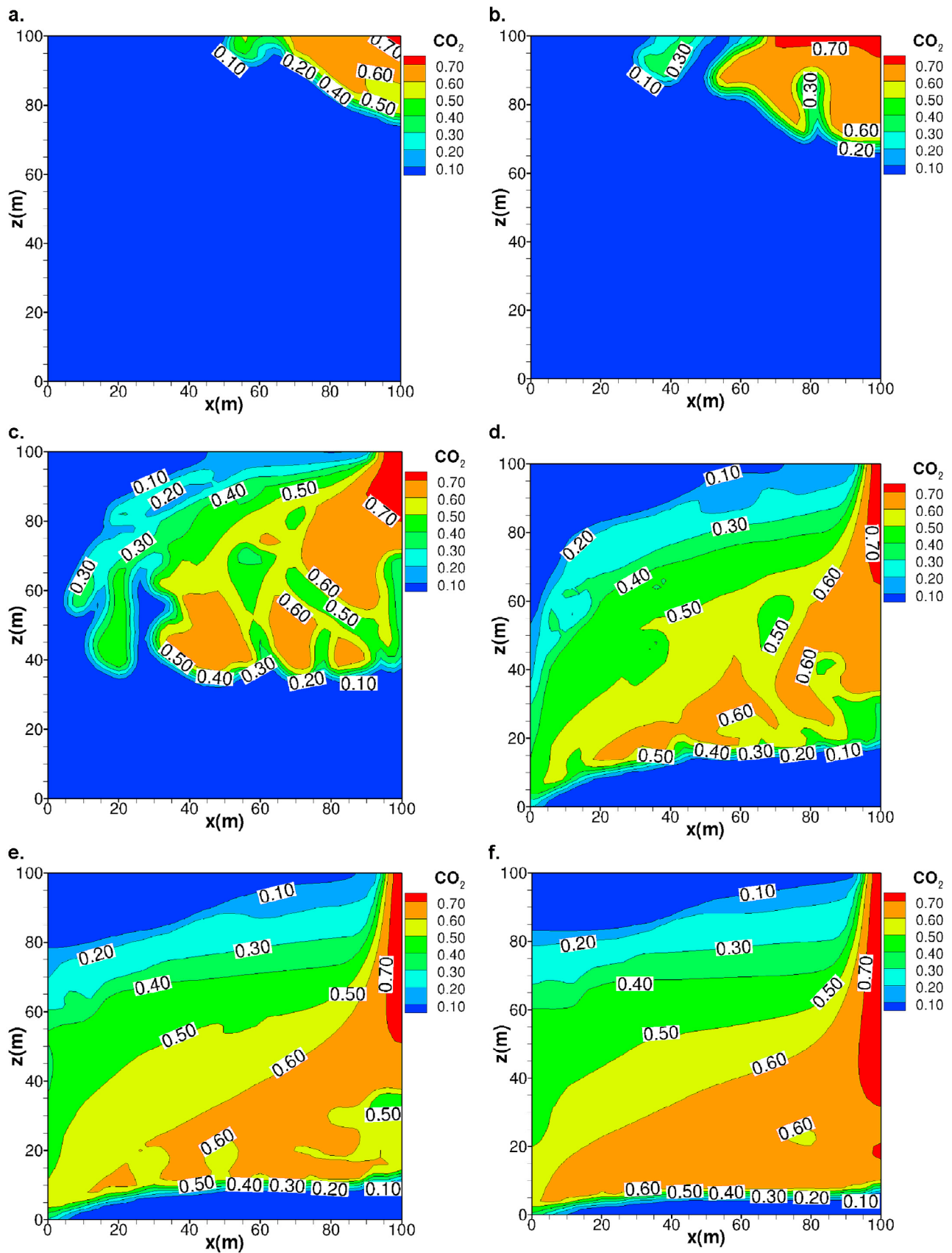| Species	z_i^0	ω	T_c(K)	p_c(bar)	M_w(g/mole)	V_c(cm^3/g)	s
CO_2	0.007	0.239	304.1	73.8	44	2.14	0.10
C_1-N_2	0.563	0.012	189.3	45.8	16	6.09	−0.16
C_2-C_3	0.154	0.120	329.9	46.3	35	4.73	−0.10
C_4-C_6	0.078	0.233	454.9	34.6	69	4.32	−0.05
C_7-C_{10}	0.091	0.429	583.9	24.3	120	4.25	0.05
C_{11+}	0.106	1.062	750.7	13.0	293	4.10	0.13

Figure 11. Example 4, showing the overall molar fraction of CO_2 at (a) 5%, (b) 10%, (c) 30%, (d) 50%, (e) 70%, and (f) 100% PV CO_2 injection.
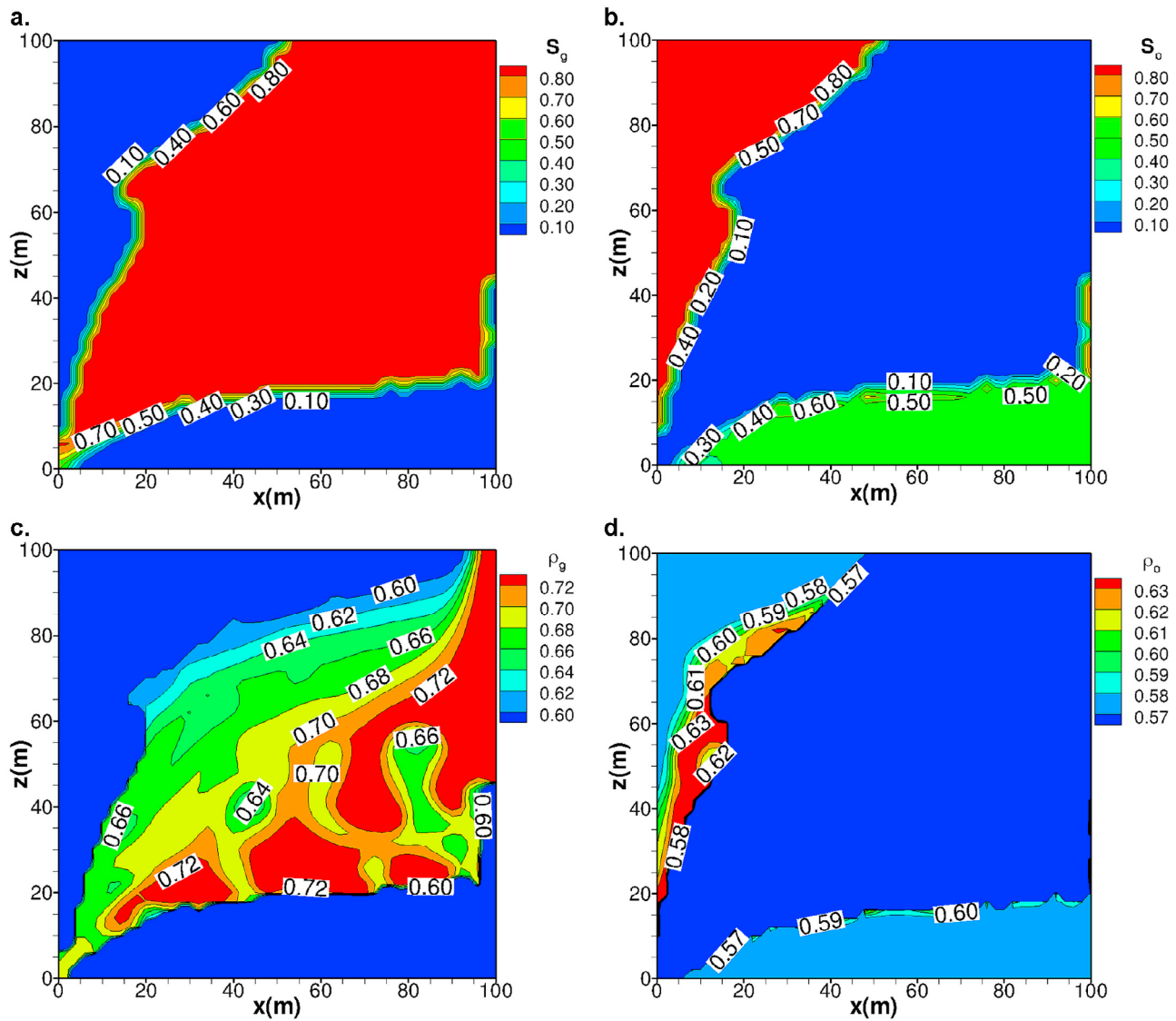
Figure 12. Example 4, showing results at 45% PV of CO_2 injection from top right corner: (a) gas and (b) oil saturation and density in g/cm^3 for (c) gas and (d) oil phases.

from the top right corner and then switch the injection and production wells and inject one PV of CO_2 from the top right corner. The difference between the next two examples is the composition of the original oil in place as well as the reservoir temperature and pressure. The injected CO_2 is lighter than the oil in example 3 and denser than the oil in example 4.

4.3. Example 3: Water Flooding and CO_2 Injection for Multicomponent Oil in Vertical 2-D Domain With $\rho_{CO_2} < \rho_o$

[71] We first consider an oil with initial composition and critical parameters listed in Table 4 comprised of of eight defined and lumped (pseudo) components. At the initial temperature of 403 K and pressure of 276.8 bar (at the bottom of the reservoir), the mass density of water, reservoir oil and CO_2 are ~0.95, 0.67 and 0.54 g/cm^3, respectively. The relative permeability parameters are listed in Table 2.

[72] Figure 6 shows the water saturation throughout the domain at 5%, 30%, 60%, and 100% PV of water injection.

Similar to the previous example, the water saturation does not increase beyond 60%, due to the residual oil saturation, and water breakthrough occurs at early times. From the recovery plot, Figure 7a, we observe that water flooding becomes ineffective after 60% PV of water injection (1.7 years). Note the horizontal spreading of the dense water due to gravity in comparing Figures 6b and 6c to Figure 4a.

[73] To enhance oil recovery and store CO_2, we inject one PV of CO_2 at a rate of 13.5% PV/yr. Because CO_2 is lighter than both the oil and the water under these reservoir conditions, the best recovery strategy is to inject CO_2 from the top of the domain, where it can spread laterally and form a gas cap that gradually pushes out the remaining oil. We therefore switch the injection and production wells and inject from the top right corner, while producing from the bottom left corner.

[74] From Figure 7a, it is clear that after a delay, the recovery is substantially enhanced, as the phase behavior effects of CO_2 mixing with the oil leads to swelling of
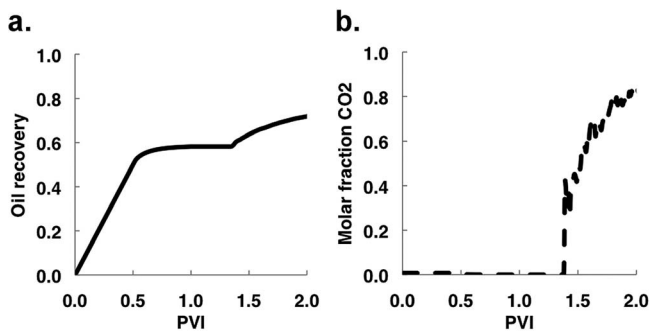
Figure 13. Example 4, showing (a) oil recovery and (b) overall molar fraction of CO_2 in the production well.

the oil volume above the residual oil saturation to water and increases mobility due to the viscosity reduction. The overall composition of CO_2, plotted in Figure 8, shows the initial development of a gas cap and continued flow at (CO_2) PVI = 5, 10, 30, 50, 70, and 100%, respectively. At the termination of injection, more than half of the injected CO_2 is stored in the reservoir.

[75] At the CO_2-oil interface, the lighter components in the oil first evaporate into the gas-phase. This results in a local decrease in the gas density and plumes of lighter gas that buoyantly flow upward, as seen in Figures 8c–8f. Figure 9 shows details of gas composition and phase density and saturation at 45% PV CO_2 injection. In Figures 9a and 9b we clearly see how methane and the pseudocomponent C_4-C_5 evaporate everywhere along the gas-oil interface and trace the observed plumes. The lower gas density of the plumes is plotted in Figure 9c. Note that a local density difference of only a few percent (~5% in this case) can induce significant upward (or downward) fingering. At the same time, a rotational component of the velocity field is driven by the different orientations of pressure gradients with respect to density gradients (this is see more clearly in animations of the complete time series).

[76] The evaporation effect into the gas-phase is readily visualized because most of the region behind the gas-oil front has a high and fairly uniform gas saturation, as shown in Figure 9d. The finger-like features in the oil density (Figure 9e) are less relevant as the oil saturation behind the front is very low (Figure 9f). More important is the overall oil density profile, which shows that the oil density is everywhere higher than the gas density, and highest where the CO_2-rich gas phase has evaporated and removed most of the lighter components in the oil.

[77] From Figures 9d and 9f for the gas and oil saturations, respectively, we see that the recovery by CO_2 injection is very efficient given the residual water saturation of 0.1, the residual oil saturation to water of 0.4 and residual oil saturation to gas of 0.1 (i.e., $S_{gmax} = 0.8$). In Figure 9e we observe an expanding circular region around the injection well whereall the oil has evaporated and the hydrocarbon fluid is in single-phase gas, similar to the previous example. Water is the densest phase and has mostly segregated to the lower part of the domain.

[78] CO_2 breakthrough occurs around $t = 6.6$ years or at ~50% PV CO_2 injection, which can be observed from Figure 7b. Figure 7b shows the mole fraction of CO_2 in the production well. After CO_2 breakthrough, the recovery rate can be seen to decrease significantly. This example illustrates some features of our new three-phase model. In a more realistic study, where the reservoir dimensions could be much larger, breakthrough could be significantly delayed, which increases the CO_2 storage capacity and results in more efficient recovery through CO_2 injection. Even in the geometry considered in this example, incremental recovery is 23% in 7.6 years.

[79] Finally, in Figure 10 we depict the results using a lowest-order FD mass transport update. Contrasting Figures 10a and 10b to Figures 8c and 8d we see that on the same mesh the DG simulation resolves many features that are washed out by the numerical diffusion of the FD method. The FD results at 30% PV CO_2 injection show no sign of the gravitational plumes that can be observed in
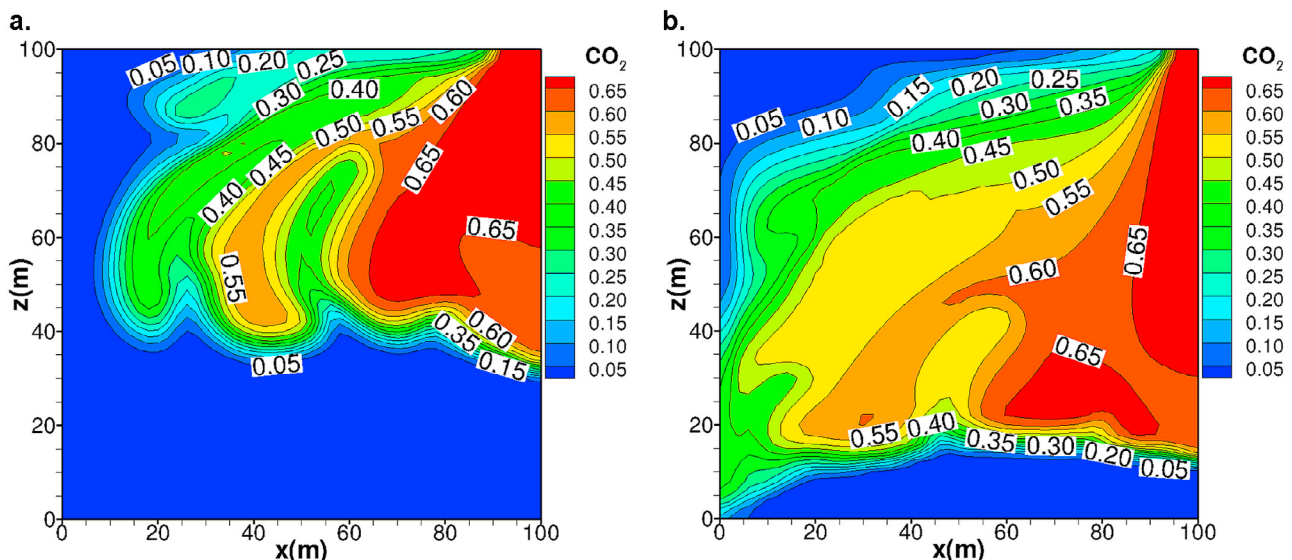

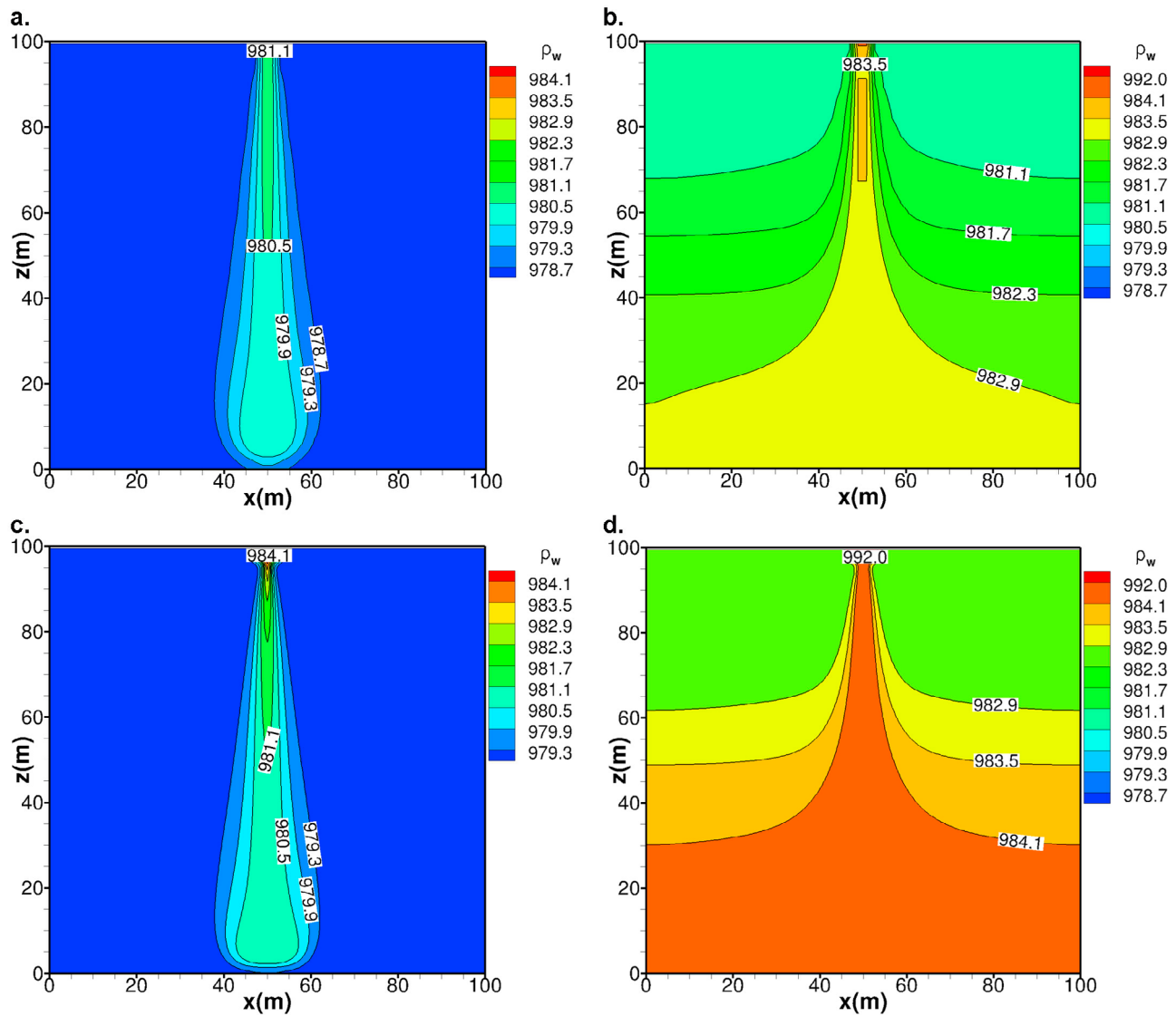**Figure 14.** Example 4, showing the overall CO_2 molar composition computed with lowest-order FD at (a) 30% and (b) 50% PVI.

Figure 15. Example 5a, showing water density (kg/m^3) at (left) 0.5% and (right) 2.0% PVI, using DG on (a and b) 50 × 50, (c and d) 180 × 180, (e and f) 200 × 200, and (g and h) 220 × 220 grids.

the DG results, where the onset of seven or eight plumes is apparent. Only after ~50% PVI do we see plumes emerge in the FD results, but due to the numerical diffusion several of the plumes that are resolved in DG (Figure 8c) are smeared out and merged into fewer, larger fingers. To converge to the same accuracy as DG, a FD simulation would have to be carried out on a substantially more refined mesh leading to orders of magnitude higher CPU times [*Hoteit and Firoozabadi*, 2005].

4.4. Example 4: Water Flooding and CO$_2$ Injection for Multicomponent Oil in Vertical 2-D Domain With $\rho_{CO_2} > \rho_o$

[80] A unique property of CO$_2$ is that it is supercritical at a wide range of conditions in subsurface reservoirs and may have a high density. In the this example, we consider a pressure of 483 bar (and 400 K temperature), such that the injected CO$_2$ has a higher density (~ 0.75 g/ cm^3) than the relatively light oil (~0.57 g/cm^3), but lower than the water density (0.96 g/cm^3). EOS and relative permeability para-

meters as well as other simulations parameters are listed in Tables 2 and 5.

[81] One pore volume of water is injected first at the same rate as in the previous example, i.e., as in Figure 6, before switching the injection and production wells and starting CO$_2$ injection from the top right corner at the same rate as before. Composition of CO$_2$ throughout the domain is shown in Figure 11 at (CO$_2$) PVI = 5, 10, 30, 50, 70, and 100%. After 5% PV injection it is already clear that the CO$_2$ is draining in the vertical direction much faster than in the previous example (Figure 11a versus Figure 8a).

[82] The purpose of this example is to show that injecting a dense fluid on top of a lighter one is unstable. This is apparent from Figure 11c, at 30% PVI. Clearly, this is not a desirable recovery strategy. It does, however, show the accuracy of our higher-order method that can capture these nonlinear instabilities (several distinct gravitational fingers in Figure 11c) and resolve the sharp fronts at the gas-oil interfaces. As the fingers are advected toward the production well, they start to merge (Figure 11d) and homogenize
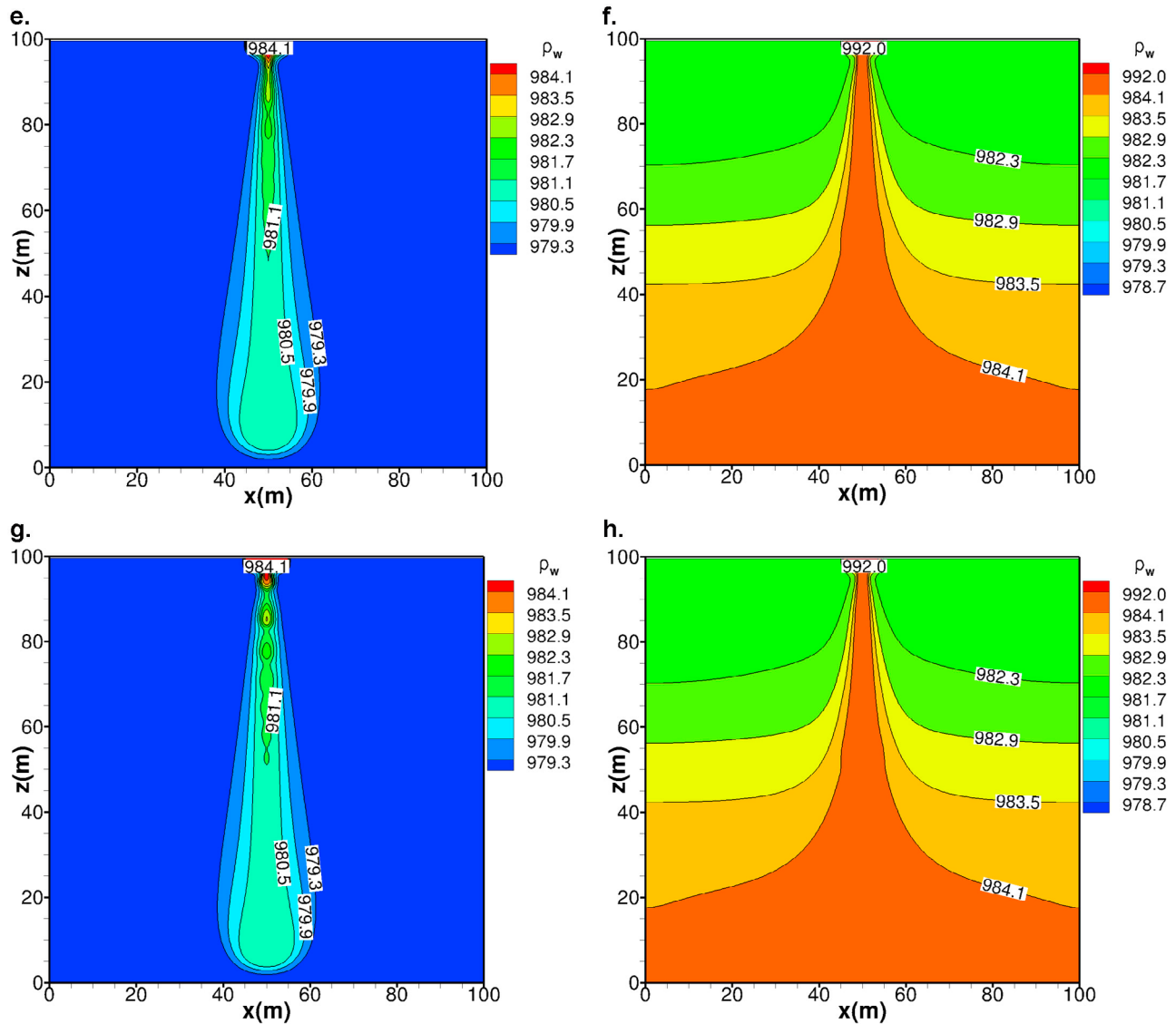
Figure 15. (continued)

as can be seen from the saturation and density distributions in Figure 12 at 45% PV CO_2 injection. This is after breakthrough, which is more clearly defined by the CO_2 composition in the production well in Figure 13b. Finally, the system settles to a more uniform quasi-steady flow (Figures 11e–11f) in which the denser gas sinks vertically from the injection well and propagates to the production well below some of the lighter oil.

[83] These two examples illustrate the importance of a thorough understanding and modeling capability of the phase behavior and gravity effects involved in three-phase recovery schemes. For identical domain size, porosity, permeability, and CO_2 injection rates, the incremental oil recovery through CO_2 injection in this example (Figure 13a) is substantially less than that in the previous example at 13% versus 23%, due to the high density of CO_2 at reservoir conditions which was 20% lower than the oil density in example 3 and 30% higher than the oil density in this example.

[84] Lowest-order FD results, in Figure 14, shows how important physical features can be obscured by over-stabilizing numerical diffusion. Several of the gravitational fingers resolved in the DG simulation (Figure 11c) are smeared out or merged in the FD simulation (Figure 14a).

[85] The simulations presented in this section were performed on a 2.8 GHz Intel Core 2 Duo iMac with *2* GB 800 MHz DDR2 SDRAM. The code was compiled with the Intel Fortran compiler with the best optimization flags and using the Pardiso linear solver included in the Intel Math Kernel Library. In these numerical examples, we have concentrated on exploring new features of the three-phase model and have used more stringent maximum time steps than required. We therefore provide only upper limits of typical CPU times, which were $T_{CPU} < 1$ min for example 1, $T_{CPU} < 3$ min for example 2 (on the 32×32 mesh), and $T_{CPU} < 1$ hr for examples 3 and 4, where the phase splitting calculations take 60–75% of CPU time.
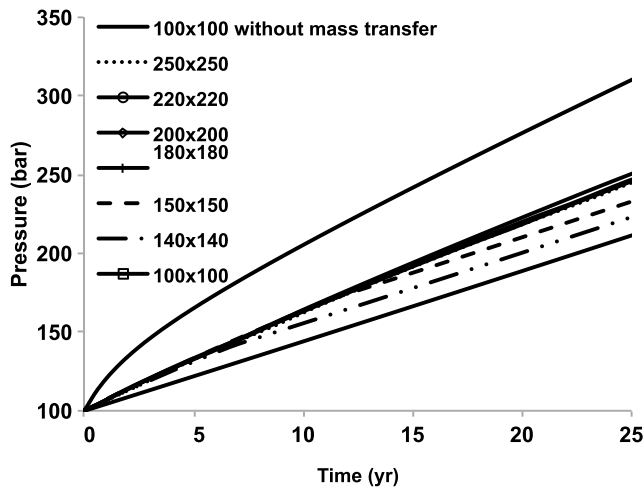
Figure 16. Example 5a, showing pressure increase in simulations on different mesh sizes, using DG methods with and without mass transfer.

4.5. Example 5: CO_2 Sequestration, Including Diffusion and CO_2 Solubility in Aqueous Phase

[86] We conclude this section with a simulation of CO_2 sequestration in an aquifer, using our higher-order accurate MHFE-DG method. Carbon sequestration is a two-phase problem. We can therefore include mass transfer and Fickian diffusion with respect to the aqueous phase, without requiring three-phase phase splitting computations. We use, for the first time, a cubic-plus-association equation of state [*Li and Firoozabadi*, 2009] to model the dissolution and phase behavior of CO_2 in water. Two-phase Fickian diffusion is modeled as in the work of *Moortgat and Firoozabadi* [2010] with a diffusion coefficient for the aqueous phase of 8×10^{-9} m^2/sec at 350 K.

[87] We consider a 100×100 m^2 vertical domain saturated with water. The initial reservoir bottom pressure is 100 bar and the temperature is 350 K. At these conditions, the CO_2 solubility in water is ~1.7 mol%. We assume a residual water saturation of 30% to CO_2, unit water and gas relative permeability end points and quadratic exponents. CO_2 is injected from the top middle (50 m, 100 m), and all boundaries are impermeable (no production well).

[88] The injected CO_2 dissolves in water and increases the density of the aqueous phase by 1% (from 0.978 g/cm^3 to 0.987 g/cm^3) at the initial condition. When the pressure increases, the solubility of CO_2 and the density effect become more pronounced. At 250 bar, the solubility is 2.5 mol% and the density increase is 1.4%, from 0.983 g/cm^3 to 0.997 g/cm^3. Even a small density increase is gravitationally unstable and may result in gravitational fingering. However, if the rock permeability is low, the fingers develop and propagate at a low rate. For high rock permeabilities, the convective mixing is most efficient and dispersion can be neglected. In this example, we consider a permeability of 5 d. A related parameter is the injection rate. At sufficiently low injection rates, all CO_2 may potentially dissolve in the water, while at higher rates a gas cap may form and the pressure increase is higher. In the next two subexamples, we inject CO_2 first at a low rate of 0.1% PV/yr and then at a 10 times higher rate of

1% PV/yr. In both examples, a total of 2.5% PV is injected (computed at 100 bar).

4.5.1. Example 5a: 0.1% PV/yr Injection

[89] When CO_2 is injected at a low enough rate, the diffusive-convective mixing process can transport the dissolving CO_2 downward before the CO_2 composition in the aqueous phase reaches the saturation level near the injection well. As a result, little or no gas cap appears and only a single gravitational finger develops below the injection well. This is illustrated in Figure 15, which shows the density of the aqueous phase after injecting 0.5 and 2.0% PV of CO_2 (computed at the initial pressure). Figure 15 also demonstrates the convergence of the results on mesh sizes of 50×50, 180×180, 200×200, and 220×220 element meshes (more mesh sizes were considered but not shown in Figure 15). While even on the coarsest 50×50 mesh the main features of the relatively uncomplicated problem are resolved, the results only fully converge on mesh sizes over 180×180.

[90] A more relevant way to quantify the converging results is given in Figure 16, which shows the pressure increase in the aquifer as a result of CO_2 sequestration. For the coarsest mesh sizes, numerical diffusion results in artificial additional mixing of CO_2 with water, which reduces the pressure increase. The pressure converges for mesh sizes of 180×180 and finer. The final pressure, after injecting 2.5% PV of CO_2 is 250 bar for these simulations. However, we have neglected rock compressibility, which may reduce the pressure increase during CO_2 sequestration.

[91] Figure 16 includes the prediction for the pressure increase when the solubility of CO_2 is neglected (the results are not sensitive to mesh size). Without mass transfer, there is no diffusive-convective mixing. Figure 17 illustrates that the injected CO_2 remains in a gas cap in the top of the aquifer, which results in the higher final pressure of 314 bar.

4.5.2. Example 5b: 1% PV/yr Injection

[92] When CO_2 is injected at a high rate, a gas cap develops over the full width of the domain and offers a large interaction surface between injected CO_2 and water. CO_2
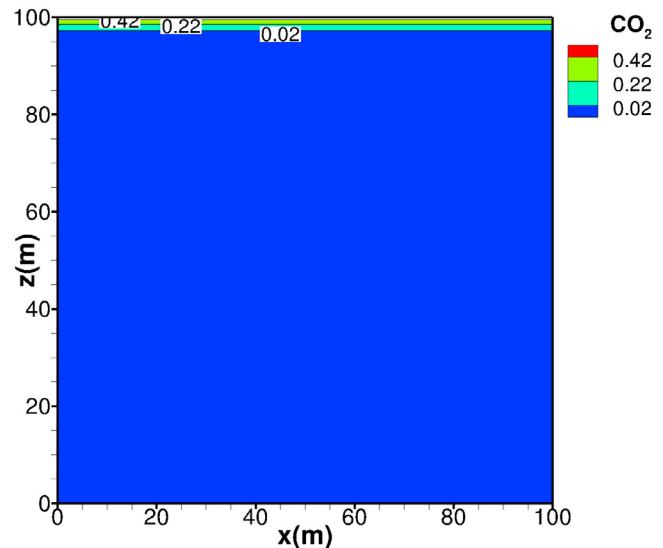

Figure 17. Example 5a, showing DG result at 2% PVI for overall molar CO_2 composition on a 50×50 element mesh without CO_2 dissolution.
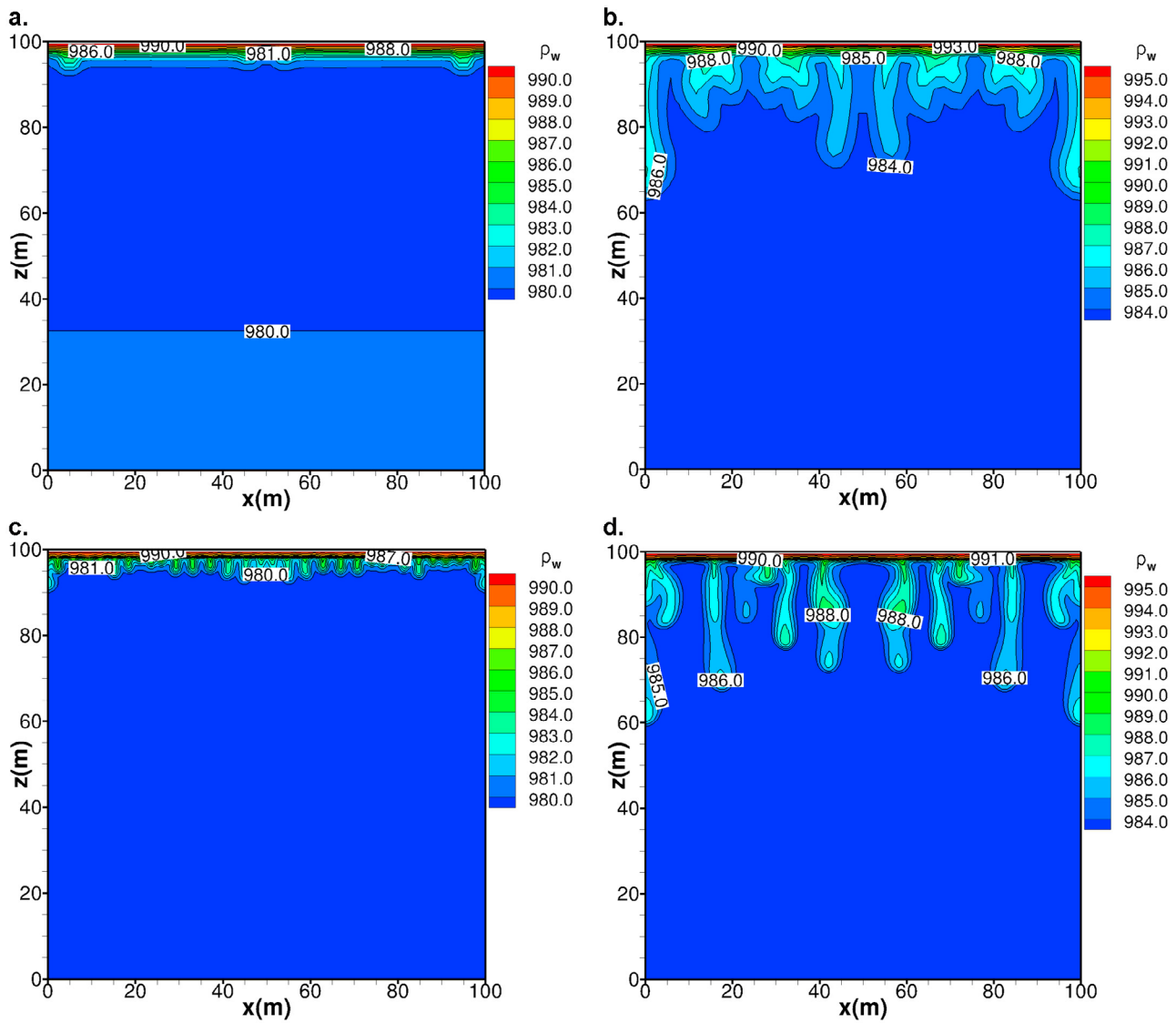
Figure 18. Example 5b, showing water density (kg/m^3) at (left) 0.5% and (right) 2.0% PVI, using DG on (a and b) 50 × 50, (c and d) 180 × 180, (e and f) 200 × 200, and (g and h) 220 × 220 grids.

dissolves in the water everywhere along this surface through Fickian diffusion. This causes a local density increase of the aqueous phase, which is gravitationally unstable. A large number of small-scale gravitational fingers appears, which prevents further growth of the gas cap.

[93] In physical systems, the initial onset of gravitational fingers is triggered by small local fluctuations in fluid or rock properties. In numerical simulations, the fingering is sometimes triggered by a prescribed artificial perturbation. We find no need for such a perturbation when using higher-order methods, which can resolve the smallest-scale fingers triggered by numerical precision errors. Because these precision errors are randomly generated and due to the highly nonlinear nature of the gravitoconvective mixing, we expect some variation in the early growth of the fingers. At later times, a steady state may be reached that is less sensitive to the initial perturbation.

[94] Convergence of the numerical results is judged by the onset time of the gravitational fingers, the number of

fingers at later times and how far they propagate downward, and most importantly, the aquifer pressure increase. We show the density of the aqueous phase after injecting 0.5 and 2.0% PV of CO_2 in Figure 18, computed on four mesh sizes. On the coarsest 50 × 50 element mesh, the initial onset of the fingers is not resolved at 0.5 PVI. On the other three meshes the smallest scale fingers are resolved at 0.5 PVI as well as 2.0% PVI. However, only mesh sizes finer than 180 × 180 converge to the same symmetry (even number of fingers at 0.5 PVI and odd at 2.0% PVI), number of fingers (13), and propagation distance (down to 65 m).

[95] The predictions for the aquifer pressure increase during sequestration are depicted in Figure 19. Even the simulation on the coarsest mesh provides a reasonable prediction of the pressure increase (as well as the fingering at 2.0% PVI in Figure 18). The convergence trend is the opposite from the previous example: from higher to lower final pressures for finer meshes. The reason is that, while in the previous example numerical diffusion resulted in some
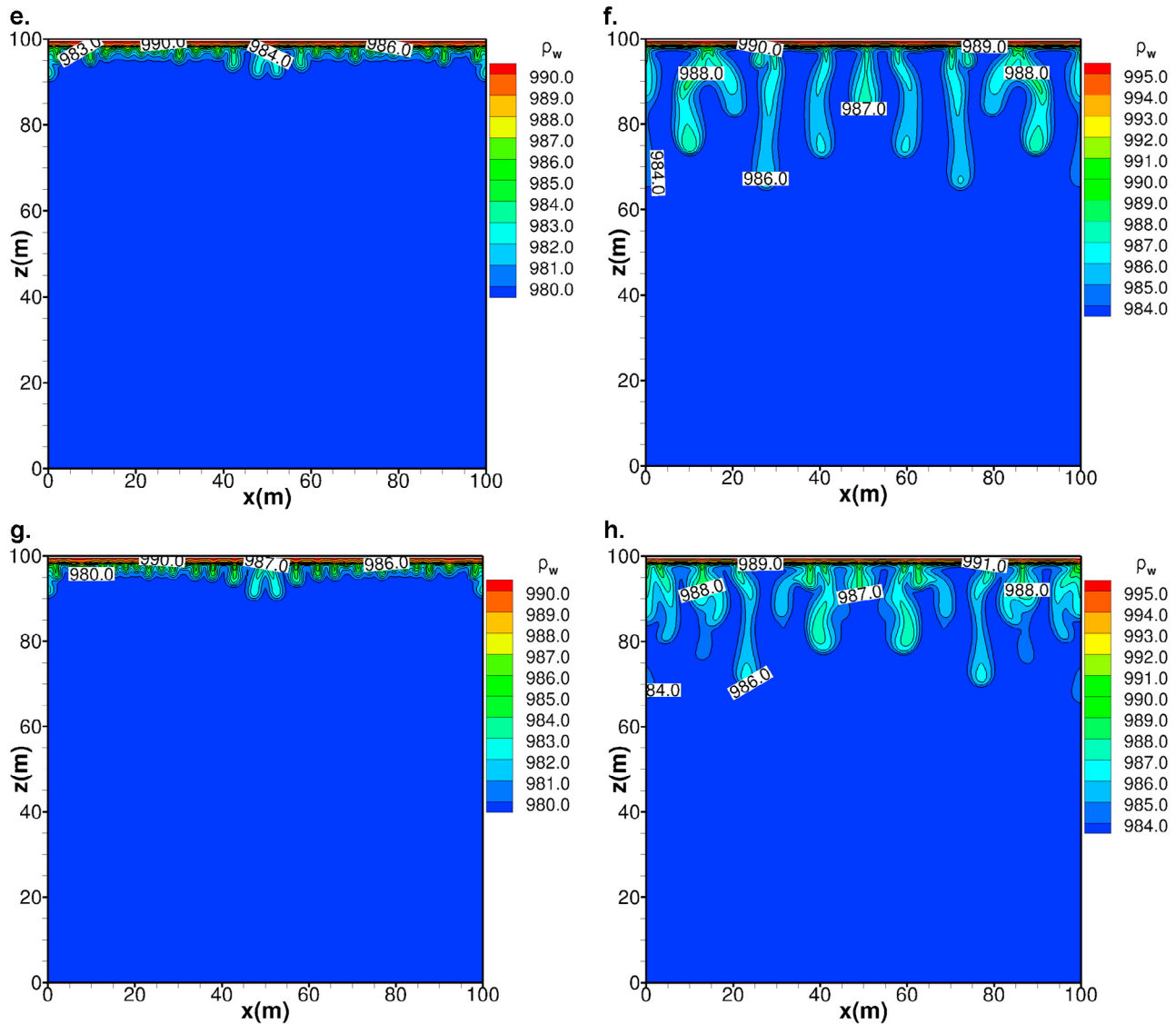
Figure 18. (continued)

additional mixing of CO_2 and water, in this example numerical diffusion delays the onset of gravitational mixing through small fingers. The final pressure is higher than for the low rate injection due to the formation of a large gas cap, but only by 14 bar, due to the development of a larger number of gravitational fingers. The considerably larger pressure increase predicted by a simulation without CO_2 dissolution is shown for comparison.

[96] Figure 20 shows the aqueous phase density at 0.5 and 2.0% PVI computed using the lowest-order mass transport update (FD) on two fine grids with 200×200 and 250×250 elements. The resolution on the 200×200 element mesh using FD is comparable to that on the 50×50 element mesh using DG but at 27 times the computational cost in CPU time. The onset of the gravitational fingers at 0.5 PVI is suppressed by the excessive numerical diffusion. Only on a 250×250 mesh does the FD method (combined with the accurate MHFE flux update) start to resolve the onset of

gravitational fingering. The number of initial fingers has not yet converged and at 2.0% PVI the fingers develop into an asymmetrical pattern. Nevertheless, the FD methods performs relatively well for these examples (the pressure increase is near the 200×200 curve in Figure 19) because the domain is homogeneous and mostly in single-phase. The use of higher-order methods becomes increasingly more compelling in heterogeneous or fractured systems and for largely multiphase flow.

4.6. Verification

[97] The two-phase process of oil displacement by water flooding agrees well with *Hoteit and Firoozabadi* [2008], in which a different formulation is developed for incompressible and noncompositional black oil-water systems. In the work of *Hoteit and Firoozabadi* [2008], example *1*, simulation results are compared to the analytical solution for the one-dimensional Buckley-Leverett problem. We can
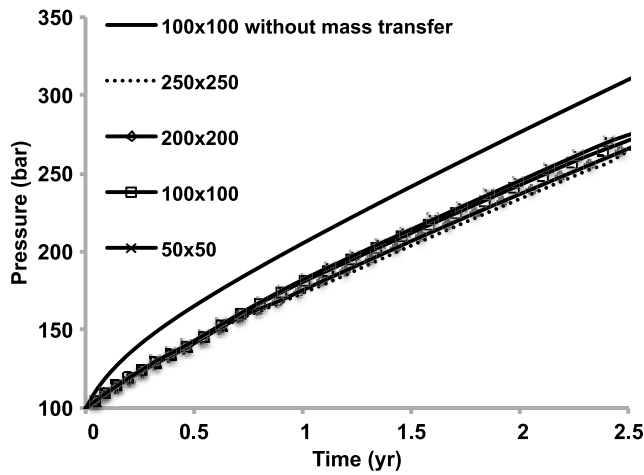
Figure 19. Example 5b, showing pressure increase in simulations on different mesh sizes, using DG methods with and without mass transfer.

accurately reproduce those results. The full three-phase behavior, presented in examples 1 and 2, was further verified with an independent MATLAB code, developed by one of the authors (S.S.), that employs a different (primal rather than hybridized) DG method for mass transport and the traditional (rather than hybridized) mixed finite element method for pressures and fluxes [*Sun et al.*, 2002]. We further reproduced the overall dynamics of examples 3 and 4 with a widely used FD commercial simulator. However, the excessive numerical diffusion inherent to the lower-order methods used in that simulator dampens much of the gravitational instabilities, comparable to the results in Figures 10 and 14.

5. Concluding Remarks

[98] This work sets the stage for three-phase flow compositional modeling based on the combined discontinuous Galerkin and mixed hybrid finite element method for a broad range of problems consisting of complicated pro-
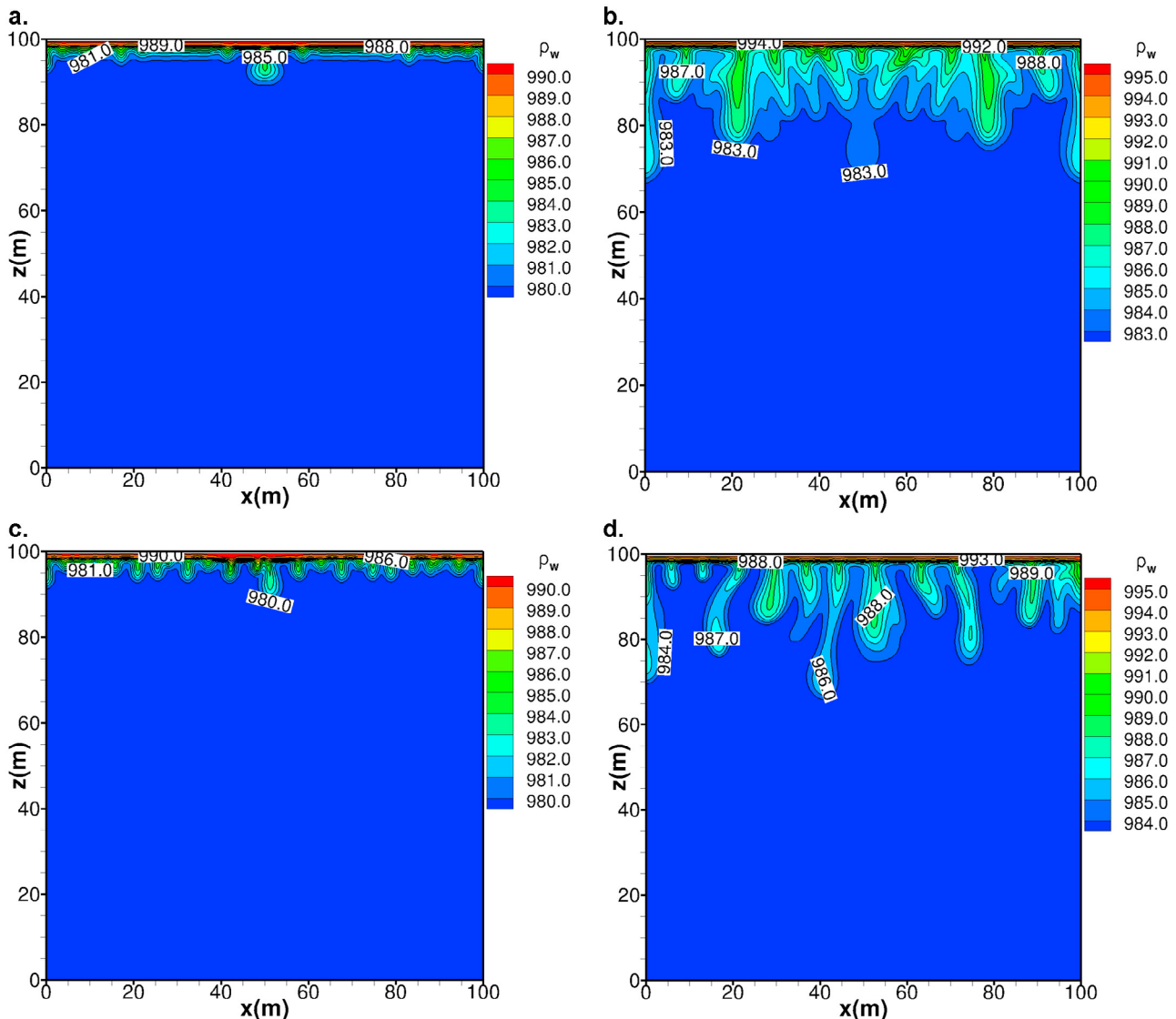

Figure 20. Example 5b, showing FD results for water density (kg/m^3) at (a) 0.5% and (b) 2.0% PVI on a 200 × 200 grid and at (c) 0.5% and (d) 2.0% PVI on a 250 × 250 grid.

cesses. For simplicity, we have neglected capillarity, mechanical dispersion, Fickian diffusion, and mass transfer between water phase and other phases in the three-phase equilibrium. We account for oil-gas phase and volumetric behavior and composition-dependent viscosity. We use the Peng-Robinson EOS to model oil-gas phase behavior, a cubic-plus-association EOS for the CO_2-water behavior, and we allow compressibility of all phases.

[99] The mathematical framework presented in section 2 consists of a transport equation for the overall molar density and composition in a three-phase fluid mixture, together with a pressure equation derived from total volume balance. Both are expressed in terms of the total volumetric flux (based on *Hoteit and Firoozabadi* [2006a]). This formalism allows for deceptively straightforward incorporation of any number of phases. Actual implementation, however, poses challenges in speed, stability, robustness, and specific issues that are resolved in this work, such as (1) working relations for partial molar volumes and compressibility of three-phase mixtures (section 2.4); (2) the incorporation of relative permeability relations (section 2.5) that are self-consistent across two-phase and three-phase regions and that take into account subtle phase behavior effects (due to which residual oil saturation to gas can lose its meaning); (3) and most importantly, the formulation of a new monotone upwinding scheme to find the upwind directions with respect to all three-phase fluxes, when only the total flux is known from the MHFE solution, and all phase fluxes may point in different directions due to gravity (section 3.4).

[100] To test our algorithm, we have compared simplified examples to other models in the literature that are either one-dimensional (analytical solution), use lower-order methods, neglect gravity or are two-phase water-oil or oil-gas models. Furthermore, the results in example 2, in particular the observed spike in nC_{10} composition, seem to agree with experiments [*Leach and Yellig*, 1981; *Kremesec and Sebastian*, 1985].

[101] The accuracy and robustness of our higher-order three-phase model is further illustrated by the examples in section 4. The numerical results show that on relatively coarse grids we can capture sharp fronts at phase boundaries and resolve small-scale phase behavior effects, such as changes in densities due to evaporation and dissolution, and the resulting (gravitational) instabilities. We compare to a lowest-order FD approximation to the transport equation (but still using the more accurate MHFE computation of the velocity field) to show how the high numerical diffusion of such methods dampens the onset of instabilities. To obtain comparable accuracy one would have to use significantly finer grids that may require orders of magnitude more CPU time. The final numerical example is a first higher-order accurate simulation of CO_2 sequestration in a water aquifer using a CPA EOS to accurately model the dissolution of CO_2 in water and subsequent phase behavior. In future work, we will incorporate capillarity, hysteresis, and full three-phase compositional modeling.

References

Acs, G., S. Doleschall, and E. Farkas (1985), General purpose compositional model, *SPE J.*, 25(4), 543–553.

Adenekan, A. E., T. W. Patzek, and K. Pruess (1993), Modeling of multiphase transport of multicomponent organic contaminants and heat in the subsurface: Numerical model formulation, *Water Resour. Res.*, 29(11), 3727–3740.

Arnold, D. (1982), An interior penalty finite element method with discontinuous elements, *SIAM J. Numer. Anal.*, 19, 742–760.

Ashcroft, S., and M. Ben Isa (1997), Effect of dissolved gases on the densities of hydrocarbons, *J. Chem. Eng. Data*, 42(6), 1244–1248.

Babuška, I. (1973), The finite element method with penalty, *Math. Comput.*, 27(112), 221–228.

Babuška, I., and M. Zlamal (1973), Nonconforming elements in the finite element method with penalty, *SIAM J. Numer. Anal.*, 10, 863–875.

Brezzi, F., and M. Fortin (1991), *Mixed and Hybrid Finite Element Methods*, Springer, New York.

Chang, Y.-B., B. K. Coats, and J. S. Nolen (1998), A compositional model for CO_2 floods including CO_2 solubility in water, *SPE Reservoir Eval. Eng.*, 1(2), 155–160.

Cockburn, B., G. E. Karniadakis, and C. E. Shu (2000), *Discontinuous Galerkin Methods, Theory, Computation, and Applications*, Springer, Berlin.

Courant, R., K. Friedrichs, and H. Lewy (1928), Partial differential equations of mathematical physics, *Math. Ann.*, 100, 32–74.

Dawson, C., S. Sun, and M. F. Wheeler (2004), Compatible algorithms for coupled flow and transport, *Comput. Meth. Appl. Mech. Eng.*, 193, 2565–1029.

Delshad, M., and G. A. Pope (1989), Comparison of the three-phase oil relative permeability models, *Transp. Porous Media*, 4, 59–83.

Delshad, M., S. G. Thomas, and M. F. Wheeler (2008a), Parallel simulations of CO_2 sequestration using a non-isothermal compositional model, paper presented at International Mechanical Engineering Congress and Exposition, Am. Soc. of Mech. Eng., Boston, Mass.

Delshad, M., S. G. Thomas, and M. F. Wheeler (2008b), Modeling CO_2 sequestration using a sequentially coupled 'Iterative-IMPEC-Time-Split-Thermal' compositional simulator, paper presented at 11th European Conference on the Mathematics of Oil Recovery, ECMOR XI, Eur. Assoc. of Geosci. and Eng., Bergen, Norway.

Delshad, M., S. G. Thomas, and M. F. Wheeler (2009), Parallel numerical simulations of non-isothermal compositional flow and chemistry, *Rep. SPE 118847*, Soc. of Petrol. Eng., Richardson, Tex.

Ewing, R. E., R. D. Lazarov, and J. Wang (1991), Superconvergence of the velocity along the gauss lines in mixed finite element methods, *SIAM J. Numer. Anal.*, 28, 1015–1029.

Falta, R. W., K. Pruess, I. Javandel, and P. A. Witherspoon (1992), Numerical modeling of steam injection for the removal of nonaqueous phase liquids from the subsurface: 1. Numerical formulation, *Water Resour. Res.*, 28(2), 433–449.

Farajzadeh, R., H. Salimi, P. L. J. Zitha, and H. Bruining (2008), Numerical simulation of density-driven natural convection in porous media with application for CO_2 injection projects, *Int. J. Heat Mass Transfer*, 50, 5054–5064.

Firoozabadi, A. (1999), *Thermodynamics of Hydrocarbon Reservoirs*, 355 pp., McGraw-Hill, New York.

Firoozabadi, A., and P. Cheng (2010), Prospects for subsurface CO_2 sequestration, *AIChE J.*, 56(6), 1398–1405.

Firoozabadi, A., D. Katz, H. Soroosh, and V. A. Sajjadian (1988a), Surface tension of reservoir crude-oil/gas systems recognizing the asphalt in the heavy fraction, *SPE J.*, 13826, 265–272.

Firoozabadi, A., R. Nutakki, T. Wong, and K. Aziz (1988b), Eos predictions of compressibility and phase behavior in systems containing water, hydrocarbons, and CO_2, *SPE Reservoir Eng.*, 3, 673–648.

Geiger, S., S. Matthäi, J. Niessner, and R. Helmig (2009), Black-oil simulations for three-components, three-phase flow in fractured porous media, *Rep. SPE 107485*, Soc. of Petrol. Eng., Richardson, Tex.

Girault, V., S. Sun, M. F. Wheeler, and I. Yotov (2008), Coupling discontinuous Galerkin and mixed finite element discretizations using mortar finite elements, *SIAM J. Numer. Anal.*, 46(2), 949–979.

Guler, B., P. Wang, M. Delshad, G. A. Pope, and K. Sepehrnoori (2001), Three- and four-phase flow compositional simulations of CO_2/NGL EOR, paper presented at Annual Technical Conference and Exhibition, Soc. of Petrol. Eng., New Orleans, La.

Hoteit, H., and A. Firoozabadi (2005), Multicomponent fluid flow by discontinuous Galerkin and mixed methods in unfractured and fractured media, *Water Resour. Res.*, 41, W11412, doi:10.1029/2005WR004339.

Hoteit, H., and A. Firoozabadi (2006a), Compositional modeling by the combined discontinuous Galerkin and mixed methods, *SPE J.*, *11*(1), 19–34.

Hoteit, H., and A. Firoozabadi (2006b), Compositional modeling of discrete-fractured media without transfer functions by the discontinuous Galerkin and mixed methods, *SPE J.*, *11*(3), 341–352.

Hoteit, H., and A. Firoozabadi (2008), Numerical modeling of two-phase flow in heterogeneous permeable media with different capillarity pressures, *Adv. Water Res.*, *31*(1), 56–73.

Hoteit, H., and A. Firoozabadi (2009), Numerical modeling of diffusion in fractured media for gas-injection and -recycling schemes, *SPE J.*, *14*(2), 323–337.

Kopp, A., P. Binning, K. Johannsen, R. Helmig, and H. Class (2010), A contribution to risk analysis for leakage through abandoned wells in geological CO_2 storage, *Adv. Water Res.*, *33*(8), 867–879.

Kremesec, V., Jr., and H. Sebastian (1985), CO_2 displacements of reservoir oils from long berea cores: laboratory and simulation results, *SPE J.*, 14306, 496–504.

Leach, M. P., and W. F. Yellig (1981), Compositional model studies—CO_2-oil displacement mechanisms, *SPE J.*, *8368*, 89–97.

Lemmon, E., M. McLinden, and D. Friend (2010), Thermophysical properties of fluid systems, in *NIST Chemistry WebBook, Stand. Ref. Database*, vol. 69, edited by P. J. Linstrom and W. G. Mallard, Natl. Inst. of Stand. and Technol., Gaithersburg, Md. (Available at http://webbook.nist.gov.)

Li, Z., and A. Firoozabadi (2009), Cubic-plus-association equation of state for water-containing mixtures: Is "cross association" necessary?, *AIChE J.*, *55*(7), 1803–1813.

Lohrenz, J., B. G. Bray, and C. R. Clark (1964), Calculating viscosities of reservoir fluids from their compositions, *J. Petrol. Technol.*, *16*(10), 1171–1176.

Mikysta, J., and A. Firoozabadi (2010), Implementation of higher-order methods for robust and efficient compositional simulation, *J. Comput. Phys.*, *229*, 2898–2913.

Moortgat, J., and A. Firoozabadi (2010), Higher-order compositional modeling with Fickian diffusion in unstructured and anisotropic media, *Adv. Water Resour.*, *33*(9), 951–968.

Nasrabadi, H., and A. Firoozabadi (2009), Complex flow and composition path in CO_2 injection schemes, *Rep. SPE 124803*, Soc. of Petrol. Eng., Richardson, Tex.

Niessner, J., and R. Helmig (2007), Multi-scale modeling of three-phase-three-component processes in heterogeneous porous media, *Adv. Water Resour.*, *30*(11), 2309–2325.

Niessner, J., and R. Helmig (2009), Multi-physics modeling of flow and transport in porous media using a downscaling approach, *Adv. Water Resour.*, *32*(6), 845–850.

Nitsche, J. (1971), Über ein Variationsprinzip zur Lösung von Dirichlet-Problemen bei verwendung von Teilräumen, die keinen Randbedingungen unterworfen sind, *Abh. Math. Sem. Univ. Hamburg*, *36*, 9–15.

Pau, G. S. H., J. B. Bell, K. Pruess, A. S. Almgren, M. J. Lijewski, and K. Zhang (2010), High-resolution simulation and characterization of density-driven flow in CO_2 storage in saline aquifers, *Adv. Water Resour.*, *33*(4), 443–455.

Peng, D.-Y., and D. B. Robinson (1976), A new two-constant equation of state, *Ind. Eng. Chem. Fundam.*, *15*(1), 59–64, doi:10.1021/i160057a011.

Raviart, P. A., and J. M. Thomas (1977), Primal hybrid finite-element methods for second-order elliptic equations, *Math. Comput.*, *31*(138), 391–413.

Reed, W., and T. Hill (1973), Triangular mesh methods for the neutron transport equation, technical report, Los Alamos Natl. Lab. Res. Libr., Los Alamos, N. M.

Rongi, L., K. Haugen, and A. Firoozabadi (2010), Convective and diffusive mixing in CO_2-liquid systems, submitted.

Simon, R., A. Rosman, and E. Zana (1978), Phase-behavior properties of CO2-reservoir oil systems, *SPE J.*, *18*(1), 20–26.

Stone, H. (1970), Probability model for estimating three-phase relative permeability, *J. Petrol. Technol.*, *214*, 214–218.

Stone, H. (1973), Estimation of three-phase relative permeability and residual oil data, *J. Can. Petrol. Technol.*, *12*, 53–61.

Sun, S., and M. F. Wheeler (2005a), Discontinuous Galerkin methods for coupled flow and reactive transport problems, *Appl. Numer. Math.*, *52*(2–3), 273–298.

Sun, S., and M. F. Wheeler (2005b), Symmetric and nonsymmetric discontinuous Galerkin methods for reactive transport in porous media, *SIAM J. Numer. Anal.*, *43*(1), 195–219.

Sun, S., and M. F. Wheeler (2006), Analysis of discontinuous Galerkin methods for multicomponent reactive transport problems, *Comput. Math. Appl.*, *52*(5), 637–650.

Sun, S., B. Riviere, and M. F. Wheeler (2002), A combined mixed finite element and discontinuous Galerkin method for miscible displacement problems in porous media, paper presented at International Symposium on Computational and Applied PDEs, Zhangjiajie Natl. Park, Zhangjiajie, China.

Wang, Y., C.-Y. Lin, C. Bidinger, V. Muralidharan, and S.-T. Lee (2003), Compositional modeling of gas injection with three hydrocarbon phases for schrader bluff eor, paper presented at Annual Technical Conference and Exhibition, Soc. of Petrol. Eng., Denver, Colo.

Watts, J. W. (1986), A compositional formulation of the pressure and saturation equations, *SPE Reservoir Eng.*, *1*(3), 243–252.

Wheeler, M. F. (1978), An elliptic collocation finite element method with interior penalties, *SIAM J. Numer. Anal.*, *15*, 152–161.

Xu, X., S. Chen, and D. Zhang (2006), Convective stability analysis of the long-term storage of carbon dioxide in deep saline aquifers, *Adv. Water Resour.*, *29*(3), 397–407.

A. Firoozabadi and J. Moortgat, Reservoir Engineering Research Institute, 595 Lytton Ave., Suite B, Palo Alto, CA 94301, USA. (af@rerinst.org; jmoortgat@rerinst.org)

S. Sun, King Abdullah University of Science and Technology, Thuwal 23955-6900, Saudi Arabia. (shuyu.sun@kaust.edu.sa)